

A PROTOTYPE PLATFORM FOR ARRAY FEED
DEVELOPMENT

by

James Richard Nagel

A thesis submitted to the faculty of

Brigham Young University

in partial fulfillment of the requirements for the degree of

Master of Science

Department of Electrical and Computer Engineering

Brigham Young University

December 2006

Copyright © 2006 James Richard Nagel

All Rights Reserved

BRIGHAM YOUNG UNIVERSITY

GRADUATE COMMITTEE APPROVAL

of a thesis submitted by

James Richard Nagel

This thesis has been read by each member of the following graduate committee and by majority vote has been found to be satisfactory.

Date

Karl F. Warnick, Chair

Date

Brian D. Jeffs

Date

Michael A. Jensen

BRIGHAM YOUNG UNIVERSITY

As chair of the candidate's graduate committee, I have read the thesis of James Richard Nagel in its final form and have found that (1) its format, citations, and bibliographical style are consistent and acceptable and fulfill university and department style requirements; (2) its illustrative materials including figures, tables, and charts are in place; and (3) the final manuscript is satisfactory to the graduate committee and is ready for submission to the university library.

Date

Karl F. Warnick
Chair, Graduate Committee

Accepted for the Department

Michael J. Wirthlin
Graduate Coordinator

Accepted for the College

Alan R. Parkinson
Dean, Ira A. Fulton College of
Engineering and Technology

ABSTRACT

A PROTOTYPE PLATFORM FOR ARRAY FEED DEVELOPMENT

James Richard Nagel

Department of Electrical and Computer Engineering

Master of Science

Radio frequency interference (RFI) is a growing problem for radio astronomers. One potential solution utilizes spatial filtering by placing an array of electrically small antennas at the focal plane of a parabolic reflector. This thesis documents the design and characterization of a prototype array feed and RF receiver that were used to demonstrate the spatial filtering principle. The array consists of a 7-element hexagonal arrangement of thickened dipole antennas tuned to a center frequency of 1600 MHz. The receiver is a two-stage, low-noise frequency mixer that is tunable over the entire L-band. This thesis also documents a new receiver design that is part of an upgrade to the outdoor antenna test range for the National Radio Astronomy Observatory in Green Bank, West Virginia.

The array feed was demonstrated on a three-meter parabolic reflector by recovering a weak signal of interest that was obscured by a strong, broadband interferer. Similar results were also obtained when the interferer moved with an angular velocity of $0.1^\circ/\text{s}$, but only when the power in the interferer dominated the signal. Using a link budget calculation, the aperture efficiency of the receiver was measured at 64%.

A measurement of pattern rumble was also carried out by comparing the SNRs of adaptive beamformers to the SNR of a fixed-weight beamformer. It was found that adaptive beamforming on a moving interferer introduces a significant amount of pattern rumble and reduces the maximum integration time by roughly one order of magnitude.

ACKNOWLEDGMENTS

I would like to extend my gratitude and appreciation to the following individuals.

Dr. Karl Warnick, for recruiting me into the project, for his guidance with my research, and patience with my learning.

Dr. Brian Jeffs, for his council and advice with my research.

Dr. Rick Fisher and Dr. Richard Bradley, for their support with my work at the NRAO.

Chris Ashworth, Micah Lilrose, and Jonathon Landon for their assistance on all of my projects.

Dr. Long and the MERS Lab, for sharing their resources, their time, and their friendship.

Joe Bussio for his council and assistance with the machine shop.

And of course, my parents, Barbara and David Nagel, for always encouraging me to work hard, study hard, and aim high.

Table of Contents

Acknowledgements	xiii
List of Tables	xix
List of Figures	xxiii
1 Introduction	1
1.1 Radio Astronomy and RFI	1
1.2 Thesis Contributions	3
1.3 Thesis Outline	3
2 Array Theory and Beamforming	5
2.1 Array Modeling	5
2.1.1 Directivity	6
2.1.2 Hertzian Dipole Model	7
2.2 Receive Arrays	7
2.2.1 Steering Vectors	8
2.3 Correlation Matrix Estimation	10
2.4 Beamforming	10
2.4.1 Maximum Gain	11
2.4.2 Maximum SINR	11
2.4.3 LCMV	12
2.4.4 Orthogonal Subspace Projection	13
2.5 Power Calibration	13

3	A Two-Stage Receiver for the Focal-Plane Array	15
3.1	Design Considerations	15
3.1.1	RFI Survey	16
3.1.2	System Overview	17
3.2	Front-End	17
3.3	Receiver Box	19
3.3.1	Band-Pass Filter	19
3.3.2	Amplifier 1 and Mixer 1	21
3.3.3	IF Stage and Mixer 2	22
3.4	Back-End	24
3.5	DC Power	25
3.6	Summary and Characterization	25
4	The Seven-Element Hexagonal Array	31
4.1	Array Geometry	31
4.2	Element Characterization	31
4.2.1	Self Impedance	34
4.2.2	Bandwidth	34
4.3	Mutual Coupling	36
4.4	Gain and Effective Area	36
5	Antenna Test Range Receiver Design for the NRAO Headquarters	41
5.1	Geometry	41
5.2	The Lock-In Amplifier	42
5.3	Theoretical Design Layout	44
5.4	LO Frequency	44
5.5	Power Losses	44
5.5.1	Line Loss	45
5.5.2	Propagation Loss	46
5.5.3	Conversion Loss	46
5.5.4	Splitter Loss	46

5.5.5	Power Budget	46
5.6	Reference Signal Bleed-Through	47
5.7	Bleed-Through Solution	48
5.8	Reference Input Power	49
5.9	Low-Pass Filters	49
5.10	Summary	49
5.11	Array Directivity Measurements	50
5.11.1	Calibration	51
5.11.2	Directivity Results	52
6	RFI Mitigation with the Focal-Plane Array	55
6.1	Experimental Setup	55
6.2	Calibration and Alignment	58
6.3	Training Data	58
6.4	Effective Area and Aperture Efficiency	59
6.5	Stationary Interferer	60
6.5.1	Single Element	60
6.5.2	Max SINR using Interferer Subspace Partitioning	61
6.6	Non-stationary Interferer	61
6.6.1	Single Element	63
6.6.2	Max SINR using Interferer Subspace Partitioning	63
6.7	Performance Versus Interferer Power	65
6.8	Correlation Time and Non-Stationarity	66
6.9	Pattern Rumble	69
7	Conclusions and Future Work	73
7.1	Robust Beamformers	73
7.2	Array Weight Normalization	73
7.3	Optimal Feed Placement	74
7.4	Mutual Coupling	74
7.5	Sensitivity	74

7.6	Array Expansion	74
7.7	Astronomical Observation on the GBT	75
	Bibliography	79

List of Tables

3.1	Receiver characterization.	28
3.2	Major parts list and power budget.	28
3.3	Minor parts list.	29

List of Figures

3.1	RFI survey results. The data was averaged for two minutes on a digital spectrum analyzer.	16
3.2	Block diagram for the radio astronomy array-feed receivers. The dashed boxes indicate the three major sections.	18
3.3	Receiver front-end.	19
3.4	Photograph of the receiver box section with the cover removed. . . .	20
3.5	Block diagram of the receiver box section. Note that each box contains two channels, labeled A and B.	20
3.6	Frequency response of the low-pass, high-pass filter combination to form a single band-pass filter.	21
3.7	SAW filter soldered into the a Mini-Circuits amplifier case. The SAW is a passive device, so the power leads are left floating.	23
3.8	Frequency response of the SAW filter.	23
3.9	Receiver back-end.	24
3.10	DC-DC regulator configuration.	26
4.1	Photograph of the prototype array feed.	32
4.2	Diagram of an array element. Each element is a balun-fed dipole with a ground-plane backing.	32
4.3	Top schematic of the prototype array.	33
4.4	Bottom schematic of the prototype array.	33
4.5	Self impedances of the array elements. The solid lines indicate real impedance while the dashed lines indicate imaginary impedance. . . .	35

4.6	Measured reflection coefficients of the 7-element array. The average center frequency is 1.61GHz, with an average reflection coefficient magnitude of -17 dB.	35
4.7	Transmission coefficient $ S_{21} ^2$ in dB for the six mutual coupling cases.	37
4.8	Experimental setup on the roof of the Clyde building used to measure the boresight gain of the 7-element array.	38
5.1	Geometry for the antenna test range. The AUT sits on top of a rotating turret, which allows the measurement of antenna gain.	42
5.2	Concept design for the single-stage lock-in receiver.	43
5.3	Revised diagram indicating the major power losses.	45
5.4	Signal path of the reference bleed-through to the SIG input.	47
5.5	An isolator made from an amplifier-attenuator pair.	48
5.6	Final design for the NRAO test-range receiver.	50
5.7	The seven-element array at the NRAO test range.	51
5.8	Co-polarized, H-plane cut pattern of the array feed compared with a theoretical Hertzian dipole model.	52
5.9	Co-polarized, E-plane cut pattern of the array feed compared with a theoretical Hertzian dipole model.	53
6.1	Rooftop positions of the antennas. The array feed and reflector are located on the roof of the Clyde Building. The horn antenna (signal) is positioned at boresight to the reflector and is located on the Kimball Tower. The interferer is a small dipole located on the observation deck of the Joseph F. Smith Building. Image taken from www.maps.google.com	56
6.2	The array feed is mounted at the focal plane of a 3-meter reflector.	57
6.3	Non-integrated PSD as seen by the center element alone. A CW signal is buried beneath the noise floor with an FM interferer overlapping. Due to baseline subtraction, the units for power are arbitrary.	62

6.4	PSD of the center element after 10 seconds of integration. The noise floor is smoothed out, but the FM interferer remains and completely masks the signal of interest.	62
6.5	PSD of the Max-SINR beamformer using interferer subspace partitioning on the stationary interferer. The total integration time is 10 seconds. Note how the interferer is almost completely removed and the signal is recovered.	63
6.6	PSD as seen by the center element after 10 seconds of integration. The interferer is traveling at a velocity of approximately $0.1^\circ/\text{s}$	64
6.7	PSD of the Max-SINR beamformer using interferer subspace partitioning on the moving interferer. The total integration time is 10 seconds. Again, the interferer is almost completely removed and the signal is recovered.	64
6.8	Interference rejection ratio of the beamformers as a function of interference to noise ratio at the center element. The red line represents $y = x$, which indicates the interferer is either at or below the noise floor.	65
6.9	Interference rejection ratio as a function of correlation length for the stationary interferer.	67
6.10	Interference rejection ratio as a function of correlation length for the moving interferer.	68
6.11	Pattern rumble for the stationary interferer. The maximum integration time is roughly 1.7 seconds.	72
6.12	Pattern rumble for the moving interferer. The maximum integration time is roughly 3.3 seconds for the fixed-weight beamformer and 0.3 seconds for the updated beamformers.	72

Chapter 1

Introduction

1.1 Radio Astronomy and RFI

Radio astronomy is the study of radio-wave signals emitted from deep space. Since these signals must travel through vast interstellar distances before reaching an observer on Earth, typical astronomical signals are extraordinarily weak. The greatest challenge in radio astronomy is therefore the detection of very faint signals that lie far beneath the background noise floor. As a consequence, radio telescopes have evolved into the most sensitive radio detection devices in the world. Unfortunately, this high sensitivity also makes radio telescopes very susceptible to spurious emissions from man-made sources. Any signal that impedes a radio astronomical observation is called radio frequency interference (RFI).

With the proliferation of devices like cellular phones, aircraft radar, and digital broadcasts, RFI is a continually growing problem among the community of radio astronomers. Even with the establishment of protected frequency bands and radio quiet zones, RFI frequently corrupts scientific observations and wastes valuable resources. Orbiting satellites present a particularly troublesome nuisance to radio astronomers, due to the fact that radio quiet zones do not apply to electronics in space. The problem is even worse when these satellites broadcast their signals in the protected bands for radio astronomy. For example, transmissions from the Russian Federation Global Navigation Satellite System (GLONASS) overlap 1612 MHz. This frequency is particularly interesting to radio astronomers, due to the resonant emissions of hydroxyl (OH) ions. To further compound the problem, much of the current

scientific interest lies outside of the protected bands for radio astronomy. Research in the unprotected bands is necessary in order to explore phenomena like high red-shift emissions, the cosmic microwave background, and the epoch of reionization.

Newer generations of radio telescopes like the Low Frequency Array (LOFAR) [1], the Allen Telescope Array (ATA) [2], and the Square Kilometer Array (SKA) [3] will be far more sensitive than their predecessors. As a consequence, RFI mitigation techniques are a vital consideration when designing new radio telescopes. Currently, the available tools for dealing with RFI include time blanking [4], parametric modeling [5], and spatial filtering [6].

The BYU radio astronomy research group is actively involved in the study of RFI mitigation for radio astronomy. Construction has been recently completed on the Very Small Array (VSA), which is a four-element synthesis array of 3 meter dishes [7]. This tool will be useful for teaching students about radio astronomy, as well as for testing new mitigation algorithms. The BYU research group has also contributed research in adaptive cancellation [8], auxiliary antenna-assisted mitigation [9], and spatial filtering with a focal-plane array [10].

The focal-plane array (FPA) is a relatively new concept for RFI mitigation. Until recently, radio astronomers have only used FPAs to perform multi-beam sky surveys and correct for reflector surface aberrations [11]. For example, the Parkes radio telescope uses an FPA that consists of 13 waveguide feeds [12], and has been successfully used for projects like the H1 Parkes all-sky survey (HIPASS) [13]. The Netherlands Foundation for Research in Astronomy (ASTRON) is working on project FARADAY, which tests the use of an array of Vivaldi antennas for multi-beam synthesis [14].

Spatial filtering offers several advantages when used in conjunction with an FPA of electrically small elements [15]. An FPA can potentially provide higher sensitivity than a conventional waveguide feed, as well as facilitate rapid sky surveys. Most importantly, an FPA can be used to spatially filter an interfering signal while still preserving high sensitivity.

1.2 Thesis Contributions

This thesis is an experimental follow-up to the numerical simulations performed by Chad Hansen, which showed that a phased array feed can be used to effectively mitigate point-source RFI [16]. Primarily, this thesis documents the design and characterization of a prototype array of seven dipole antennas arranged in a hexagonal grid. The array is also shown to be capable of recovering a weak signal of interest in the presence of a strong, FM interferer when installed at the focal plane of a 3 meter reflector.

Another contribution of this thesis is the replacement of the previous receivers that have been used with the VSA. Because the prototype FPA required its own set of receivers, it was convenient to design them as an upgrade to the previous set used by the VSA [17]. In particular, the old receivers suffered from high cross talk between channels and a poor choice of intermediate frequency (IF). A further complication also arose from the Pentek DSP, which suffers from frequent errors and a steep learning curve to operate. The new receivers solve all of these problems through the use of connectorized components, a new IF, and an analog to digital converter run by a desktop computer.

A final contribution is the demonstration of a new receiver design for our collaborators at the National Radio Astronomy Observatory (NRAO). The new receiver is part of an upgrade to the outdoor antenna test range at the NRAO headquarters in Green Bank, WV. Currently, the system is only capable of measuring the directivity of a single antenna, but FPA research requires a system that is capable of measuring the directivity of an entire antenna array. This thesis documents a new receiver design that was demonstrated on the NRAO outdoor antenna test range to measure the directivity of the prototype array.

1.3 Thesis Outline

This thesis is organized as follows:

Chapter 2, *Array Theory and Beamforming*, provides a basic mathematical introduction to array theory and beamformer theory. It also covers many of the

popular beamformers used in practice as well as some practical considerations of each.

Chapter 3, *A Two-Stage Receiver for the Focal Plane Array*, covers the design and characterization of the receivers used with the array feed. It also includes a documentation of all the important devices used to construct the receivers. Another useful feature is an RFI survey of the Provo/Orem area.

Chapter 4, *The Seven-Element Hexagonal Array Feed*, documents the geometry and characterization of the prototype FPA. It also includes measurements of bandwidth, mutual coupling, and boresight gain.

Chapter 5, *Antenna Test Range Receiver Design for the Nation Radio Astronomy Observatory*, describes a new receiver design that is intended to upgrade the current system in place at the NRAO headquarters in Green Bank, WV. The design is demonstrated on the array feed by taking multiple directivity measurements and comparing them with a theoretical model.

Chapter 6, *RFI Mitigation with the Focal Plane Array*, documents the procedure for an on-reflector experiment with the prototype FPA. It also includes a measurement of effective area and aperture efficiency of the array feed when used in conjunction with a parabolic reflector. Spatial filtering is then demonstrated by recovering of a weak signal of interest in the presence of a strong interferer. The chapter then finishes by characterizing the pattern rumble introduced by adaptive beamforming.

Chapter 7, *Conclusions and Future Work*, summarizes the important points of this thesis and provides several suggestions for future research with the focal plane array.

Chapter 2

Array Theory and Beamforming

This chapter presents a brief introduction to array theory and beamformer terminology. The purpose is to provide a theoretical framework that will be used to model the prototype array feed, as well as a quick reference about beamforming. A presentation of some of the more common beamformers is also included, and the interested reader is referred to [18] for greater details.

2.1 Array Modeling

For an array of N identical antennas in free space, each driven with a relative excitation I_n and located at the points $\mathbf{r}_1, \dots, \mathbf{r}_N$, the electric far-field \mathbf{E}_{ff} in the direction (θ, ϕ) is given in spherical coordinates as

$$\mathbf{E}_{ff}(\theta, \phi) = \mathbf{E}_e(\theta, \phi) \sum_{n=1}^N I_n e^{jk\hat{\mathbf{r}} \cdot \mathbf{r}_n} \quad (2.1)$$

where $\mathbf{E}_e(\theta, \phi)$ is the individual element pattern under unit excitation, k is the wavenumber, and $\hat{\mathbf{r}}$ is a unit vector that points in the direction of (θ, ϕ) . In rectangular coordinates, $\hat{\mathbf{r}}$ is given as

$$\hat{\mathbf{r}} = \sin \theta \cos \phi \hat{\mathbf{x}} + \sin \theta \sin \phi \hat{\mathbf{y}} + \cos \theta \hat{\mathbf{z}} . \quad (2.2)$$

A more compact form of Equation 2.1 is obtained by defining the *array weight vector* \mathbf{w} and the *steering vector* $\mathbf{d}(\theta, \phi)$ such that

$$\mathbf{w}^H = [I_1, I_2, \dots, I_N] \quad (2.3)$$

and

$$\mathbf{d}(\theta, \phi) = [e^{jk\hat{\mathbf{r}} \cdot \mathbf{r}_1}, e^{jk\hat{\mathbf{r}} \cdot \mathbf{r}_2}, \dots, e^{jk\hat{\mathbf{r}} \cdot \mathbf{r}_N}]^T . \quad (2.4)$$

Substituting back into Equation 2.1 gives

$$\mathbf{E}_{ff}(\theta, \phi) = \mathbf{E}_e(\theta, \phi) \mathbf{w}^H \mathbf{d}(\theta, \phi) . \quad (2.5)$$

Note that vectors \mathbf{E} and \mathbf{r} represent three-dimensional vectors in space, while vectors \mathbf{w} and \mathbf{d} are N-dimensional vectors corresponding to the array elements.

2.1.1 Directivity

The *directivity* D of any antenna or antenna array is defined by the quantity

$$D(\theta, \phi) = \frac{S(\theta, \phi)}{P_{rad}/(4\pi r^2)} \quad (2.6)$$

where S is the time-averaged radiated power density at (θ, ϕ) and P_{rad} is the total radiated power. For a plane wave propagating in free space, S is given as

$$S(\theta, \phi) = \frac{1}{2\eta} |\mathbf{E}_{ff}(\theta, \phi)|^2 \quad (2.7)$$

where $\eta = 377 \Omega$ is the intrinsic impedance of free-space. Using Equation 2.5, this can be written as

$$S(\theta, \phi) = \frac{1}{2\eta} |\mathbf{E}_e(\theta, \phi)|^2 \mathbf{w}^H \mathbf{B}(\theta, \phi) \mathbf{w} \quad (2.8)$$

where $\mathbf{B}(\theta, \phi)$ is an $N \times N$ matrix defined as

$$\mathbf{B}(\theta, \phi) = \mathbf{d}(\theta, \phi) \mathbf{d}^H(\theta, \phi) . \quad (2.9)$$

The total radiated power P_{rad} is found by the integrating the radiated power density over a sphere Ω with radius r , such that

$$P_{rad} = \iint_{\Omega} S(\theta, \phi) r^2 \sin(\theta) d\theta d\phi . \quad (2.10)$$

Plugging Equations 2.5 and 2.7 into Equation 2.10 yields a compact matrix equation of the form

$$P_{rad} = P_{el} \mathbf{w}^H \mathbf{A} \mathbf{w} . \quad (2.11)$$

P_{el} is defined as the total radiated power of a single, isolated element, and is given as

$$P_{el} = \frac{1}{2\eta} \iint_{\Omega} |\mathbf{E}_{el}(\theta, \phi)|^2 r^2 \sin(\theta) d\theta d\phi . \quad (2.12)$$

The matrix \mathbf{A} is called the *pattern overlap matrix* and has elements given by

$$A_{mn} = \frac{1}{2\eta P_{el}} \iint_{\Omega} e^{jk\hat{\mathbf{r}} \cdot (\mathbf{r}_m - \mathbf{r}_n)} \mathbf{E}_e(\theta, \phi) \cdot \mathbf{E}_e^*(\theta, \phi) r^2 \sin(\theta) d\theta d\phi . \quad (2.13)$$

Using Equations 2.1 through 2.13, it is possible to numerically model any arbitrary array of antennas in free space. To simulate the presence of a ground plane near the array, the image theorem is applied by introducing an identical array in free space on the opposite side of the ground plane. For any component of an element polarization that is parallel to the ground plane, its corresponding image is simply driven with a negative amplitude. Such a model will provide a quantitative theoretical comparison to use against the prototype array in chapters 4 and 5.

2.1.2 Hertzian Dipole Model

The prototype array feed, introduced in Chapter 4, consists of seven co-polarized dipole antennas above a ground plane. A useful analytical model is therefore the *Hertzian dipole*, which has closed-form expressions for the electric field radiation pattern and represents a close approximation to the field pattern of a real dipole antenna. For a $\hat{\mathbf{y}}$ -directed Hertzian dipole. The individual element pattern is given by [19]

$$\mathbf{E}_e(\theta, \phi) = -j\omega k \mu_0 I_e l \left(\hat{\boldsymbol{\theta}} \cos \theta \sin \phi + \hat{\boldsymbol{\phi}} \cos \phi \right) \frac{e^{-jkr}}{4\pi r} \quad (2.14)$$

where μ_0 is the magnetic permeability of free space, I_e is a unit excitation current, l is the dipole length, and r is the distance from the antenna. This model will be used in Chapter 5 as a comparison against the directivity measurements of the prototype array.

2.2 Receive Arrays

When an antenna array is used as a receiver instead of a transmitter, it is more appropriate to consider array theory from a signal processing perspective than from an electromagnetic perspective. Although many of the concepts are analogous to the case of a transmit array, there are many subtle differences that require careful distinction.

Begin by defining a complex random vector $\mathbf{x} = [x_1 \dots x_N]^T$ to represent complex voltage samples from each array element at a single instant in time. A *beamformer* is determined by the complex vector $\mathbf{w} = [w_1 \dots w_N]^T$ of array weights that are used to generate a linear combination of the samples from each array element. The final instantaneous output signal y is therefore a complex random variable given by

$$y = \mathbf{w}^H \mathbf{x} . \quad (2.15)$$

The average power at the output of the beamformer is then given by

$$P_{avg} = E [|y|^2] = \mathbf{w}^H \mathbf{R}_{xx} \mathbf{w} \quad (2.16)$$

where the operator $E[\cdot]$ denotes the expected value. Assuming \mathbf{x} is wide-sense stationary over time, the sample correlation matrix \mathbf{R}_{xx} is defined as

$$\mathbf{R}_{xx} = E [\mathbf{x}\mathbf{x}^H] . \quad (2.17)$$

Note that for a zero-mean random process, the correlation matrix is equivalent to the covariance matrix. The diagonal elements of \mathbf{R}_{xx} represent the variances of each array element and the off-diagonal elements represent the cross-correlations between array elements.

A useful model for the random vector \mathbf{x} is the superposition of random vectors from a signal of interest (SOI) \mathbf{x}_s , an interferer \mathbf{x}_i , and noise \mathbf{x}_n , such that

$$\mathbf{x} = \mathbf{x}_s + \mathbf{x}_i + \mathbf{x}_n . \quad (2.18)$$

If the three components are all mutually independent of each other, then the sample correlation matrix \mathbf{R}_{xx} can likewise be expressed as a superposition of the signal correlation matrix \mathbf{R}_{ss} , the interferer correlation matrix \mathbf{R}_{ii} , and the noise correlation matrix \mathbf{R}_{nn} , such that

$$\mathbf{R}_{xx} = \mathbf{R}_{ss} + \mathbf{R}_{ii} + \mathbf{R}_{nn} . \quad (2.19)$$

2.2.1 Steering Vectors

In many cases of interest, the SOI and the interferer are plane waves arriving from point sources in fixed directions. Under these conditions, the random vectors

\mathbf{x}_s and \mathbf{x}_i can be written as

$$\mathbf{x}_s = x_s \mathbf{d}_s \quad \text{and} \quad (2.20)$$

$$\mathbf{x}_i = x_i \mathbf{d}_i . \quad (2.21)$$

The quantities x_s and x_i are random variables that represent the instantaneous amplitudes of the signal and interferer. Analogous to Equation 2.22, \mathbf{d}_s and \mathbf{d}_i are *steering vectors* or *array response vectors*, and represent the relative responses of each array element to the incident plane wave.

In practice, it is rare for the array element responses to be perfectly identical. For example, the receiver channels may not have identical voltage gains, and the presence of a reflector will unevenly distribute the incident plane wave among the antenna elements. To take this into account, the steering vector is modified from Equation 2.22 and instead written as

$$\mathbf{d} = [A_1 e^{j\phi_1}, A_2 e^{j\phi_2}, \dots, A_N e^{j\phi_N}]^T \quad (2.22)$$

where A_n represents the relative amplitude at element n and ϕ_n represents the relative phase.

From Equation 2.17, any incident plane wave defined by $\mathbf{x} = x\mathbf{d}$ also corresponds to a rank-one correlation matrix \mathbf{R} , given as

$$\mathbf{R} = \sigma^2 \mathbf{d}\mathbf{d}^H \quad (2.23)$$

where $\sigma^2 = \text{E}[x^2]$ is the average power in the signal. In this form, it can be shown that \mathbf{d} is the *principle eigenvector* of \mathbf{R} , meaning that \mathbf{d} is the eigenvector of \mathbf{R} corresponding to the maximum eigenvalue. The proof is found in the eigen equation,

$$\mathbf{R}\mathbf{v} = \sigma^2 \mathbf{d}\mathbf{d}^H \mathbf{v} = \lambda \mathbf{v} \quad (2.24)$$

where \mathbf{v} represents an eigenvector of the matrix \mathbf{R} and λ is the corresponding eigenvalue. Note that the quantity $\sigma^2 \mathbf{d}\mathbf{d}^H \mathbf{v}$ is some arbitrary scalar, so it can be replaced with the constant α such that

$$\alpha \mathbf{d} = \lambda \mathbf{v} . \quad (2.25)$$

Since any nonzero scalar multiple of an eigenvector is also an eigenvector, the steering vector \mathbf{d} is an eigenvector of the matrix \mathbf{R} . Also, because the matrix \mathbf{R} is rank-one, scalar multiples of \mathbf{d} are the only possible eigenvectors. The usefulness of this result is that in the case of a single, dominant signal, the steering vector can be approximated by the principle eigenvector of the sample correlation matrix.

2.3 Correlation Matrix Estimation

An important figure of merit to any beamformer is the amount of knowledge that is required about steering vectors and correlation matrices in order to form a solution. This information must either be computed from the observed data or known *a priori*, and the usefulness of a particular beamformer often depends on the availability of such information.

In practice, \mathbf{R}_{ss} and \mathbf{R}_{nn} are the most stable and therefore the most practical to implement using *a priori* knowledge. For example, in the absence of an interferer, the matrix \mathbf{R}_{ss} can be obtained by pointing the array at a strong, coherent source. The sampled data will then be dominated by the SOI, which can then be used to calculate \mathbf{R}_{ss} . The matrix \mathbf{R}_{nn} can also be measured by pointing the array at an empty region of the sky. This minimizes any coherent signals and the sampled data will be dominated by the background noise. As long as the gain and phase characteristics of the receiver are stable, \mathbf{R}_{ss} and \mathbf{R}_{nn} will also be stable.

The interferer correlation matrix \mathbf{R}_{ii} is generally impractical to obtain *a priori*. The reason is because interference tends to originate from random, non-stationary directions, therefore making \mathbf{R}_{ii} unstable. Unless estimates for \mathbf{R}_{ii} can be rapidly updated, statistical variation can degrade its usefulness after just a few seconds. However, if power in the interferer is much stronger than the signal or noise, then estimates for \mathbf{R}_{ii} can be obtained from the sample data itself.

2.4 Beamforming

The next several sections provide a summary of the more common beamformers, as well a few notes on their usefulness and implementation.

2.4.1 Maximum Gain

One of the simplest beamformer algorithms is to maximize gain in the direction of the SOI. In array processing terms, this is equivalent to maximizing the signal-to-noise ratio (SNR) from a given direction, where SNR is written as

$$\text{SNR} = \frac{\mathbf{w}^H \mathbf{R}_{ss} \mathbf{w}}{\mathbf{w}^H \mathbf{R}_{nn} \mathbf{w}} . \quad (2.26)$$

Maximization of Equation 2.26 results in an eigenvalue problem of the form

$$\mathbf{R}_{nn}^{-1} \mathbf{R}_{ss} \mathbf{w} = (\text{SNR}) \mathbf{w} . \quad (2.27)$$

Thus, SNR is maximized if the weight vector is the principle eigenvector of Equation 2.27. This solution is called the *max-gain* or *max-SNR* beamformer.

If the SOI is a point source, then a more direct solution can be obtained by substituting $\mathbf{R}_{ss} = \sigma^2 \mathbf{d}_s \mathbf{d}_s^H$ and solving for \mathbf{w} ,

$$\mathbf{w} = \frac{\mathbf{R}_{nn}^{-1} \sigma^2 \mathbf{d}_s \mathbf{d}_s^H \mathbf{w}}{(\text{SNR})} . \quad (2.28)$$

Now substitute the constant

$$\alpha = \frac{\sigma^2 \mathbf{d}_s^H \mathbf{w}}{(\text{SNR})} \quad (2.29)$$

and the result is

$$\mathbf{w} = \alpha \mathbf{R}_{nn}^{-1} \mathbf{d}_s . \quad (2.30)$$

Note that the constant α has no effect on the final SNR, but only has the effect of scaling the final output signal y (see Section 2.5). It can therefore be dropped from Equation 2.31 to yield

$$\mathbf{w} = \mathbf{R}_{nn}^{-1} \mathbf{d}_s . \quad (2.31)$$

Any adaptive beamformer of this form is called a *Capon* beamformer.

2.4.2 Maximum SINR

The beamformer we are most interested in is the one that maximizes the ratio of signal power to interference-plus-noise power. Defining the matrix $\mathbf{R}_{NN} = \mathbf{R}_{ii} + \mathbf{R}_{nn}$, the signal to interference-plus-noise ratio (SINR) is defined as

$$\text{SINR} = \frac{\mathbf{w}^H \mathbf{R}_{ss} \mathbf{w}}{\mathbf{w}^H \mathbf{R}_{NN} \mathbf{w}} . \quad (2.32)$$

Just like Equation 2.26, Equation 2.32 can be maximized to produce an eigenvalue problem of the form

$$\mathbf{R}_{NN}^{-1}\mathbf{R}_{ss}\mathbf{w} = (\text{SINR})\mathbf{w} . \quad (2.33)$$

Using the same procedure as in Section 2.4.1, the ideal weight vector is found to be

$$\mathbf{w} = \mathbf{R}_{NN}^{-1}\mathbf{d}_s . \quad (2.34)$$

This solution is called the *maximum-SINR* beamformer. Note that in the absence of any interferers, Equation 2.34 reduces to Equation 2.31.

An important difference between Equation 2.34 and Equation 2.31 is the presence of \mathbf{R}_{ii} in the inverted matrix. Because \mathbf{R}_{ii} is a rank-one matrix,¹ \mathbf{R}_{NN} will be ill-conditioned if the power in the interferer dominates the noise. In such a case, it is preferable to rewrite Equation 2.32 as a *generalized* eigenvalue problem of the form

$$\mathbf{R}_{ss}\mathbf{w} = (\text{SINR})\mathbf{R}_{NN}\mathbf{w} . \quad (2.35)$$

The ideal weight vector is therefore the principle eigenvector of Equation 2.35. The benefit of using this approach is an increase in numerical stability because it does not require the inversion of an ill-conditioned matrix.

2.4.3 LCMV

Another useful beamformer is one that minimizes the total output variance of a signal, but subject to a constraint,

$$\arg \min_{\mathbf{w}} \mathbf{w}^H \mathbf{R}_{xx} \mathbf{w} \quad \text{subject to} \quad \mathbf{C}^H \mathbf{w} = \mathbf{f} \quad (2.36)$$

where \mathbf{C} is a list of steering vectors and \mathbf{f} is a vector of constraints specifying the relative gain in each direction. This algorithm is called *linearly constrained minimum variance* (LCMV).

In most cases of interest, there is usually only a single constraint \mathbf{d}_s for the SOI. Equation 2.36 can therefore be rewritten as

$$\arg \min_{\mathbf{w}} \mathbf{w}^H \mathbf{R}_{xx} \mathbf{w} \quad \text{subject to} \quad \mathbf{d}_s^H \mathbf{w} = 1 . \quad (2.37)$$

¹ This is only true for a single point-source interferer. In the case of multiple interferers, \mathbf{R}_{ii} can have higher rank.

Using a Lagrange multiplier, the solution to Equation 2.36 is found to be

$$\mathbf{w} = \mathbf{R}_{xx}^{-1} \mathbf{d}_s . \quad (2.38)$$

Equation 2.38 is also referred to as the *minimum variance distortionless response* (MVDR) beamformer. The advantage of this beamformer is the lack of an interferer correlation matrix \mathbf{R}_{ii} , which is difficult to obtain *a priori*. It can also be shown that, under stationary conditions, the single-constraint LCMV solution is identical to the max-SINR beamformer [16].

2.4.4 Orthogonal Subspace Projection

For any vector \mathbf{d}_i , there exists a *projection matrix* \mathbf{P}_i that projects orthogonally onto the range of \mathbf{d}_i [20], and is given by

$$\mathbf{P}_i = \mathbf{d}_i (\mathbf{d}_i^H \mathbf{d}_i)^{-1} \mathbf{d}_i^H . \quad (2.39)$$

If \mathbf{P}_i is a projection onto a closed subspace, then the matrix

$$\mathbf{P}_i^\perp = \mathbf{I} - \mathbf{P}_i \quad (2.40)$$

is also a projection matrix, but onto a subspace that is orthogonal to the span of \mathbf{d}_i . Thus, the vector given by

$$\mathbf{w} = \mathbf{P}_i^\perp \mathbf{d}_s \quad (2.41)$$

is a projection of \mathbf{d}_s onto a subspace that is orthogonal to the span of \mathbf{d}_i . This beamformer is called *orthogonal subspace projection* (OSP).

2.5 Power Calibration

In order for the final output power P_{out} to have meaningful units, the output to the beamformer must be properly scaled. Although this is not necessary to the actual beamforming, it is important when using the array as a *radiometer*, which is a device that measures the incident power density S_{inc} due to a point source of interest. The output power P_{out} as seen by the array is then related to S_{inc} by

$$P_{out} = \eta_{pol} A_{eff} S_{inc} \quad (2.42)$$

where A_{eff} is the *effective area* of the array and η_{pol} is the *polarization efficiency* of the array. Intuitively, the quantity A_{eff} represents an equivalent area over which all energy from an incident plane wave is absorbed. The quantity η_{pol} represents the relative alignment in polarization between the array and the incident signal. For example, if the incident signal is a plane wave that is co-polarized with the array elements, then $\eta_{pol} = 1$. Typically, however, an incident signal from deep space will have a random, uniformly distributed polarization, and η_{pol} assumes a value of 0.5.

From Equation 2.16, the output power¹ as seen by the array is proportional to the average power in the sampled signal,

$$P_{out} = \frac{1}{\alpha} \mathbf{w}^H \mathbf{R}_{ss} \mathbf{w} . \quad (2.43)$$

The normalization constant α performs two functions and can be represented as a separable contribution from each,

$$\alpha = \alpha_1 \alpha_2 . \quad (2.44)$$

The constant α_1 represents a physical normalization due to the receiver gain g_r , the characteristic impedance of the transmission lines Z_0 , and the radiation resistance R_{rad} of the antenna, such that

$$\alpha_1 = \frac{|g_r|^2 |Z_0|^2}{R_{rad}} . \quad (2.45)$$

The constant α_2 represents the array weight normalization that prevents \mathbf{w} from adding or subtracting any power to the final output signal [21],

$$\alpha_2 = \mathbf{w}^H \mathbf{A} \mathbf{w} \quad (2.46)$$

where \mathbf{A} is the pattern overlap matrix defined by Equation 2.13. Thus, if P_{out} , η_{pol} , and S_{inc} are known, then it is possible to measure the effective area of the array. This technique will be used in Section 4.4 to measure the effective area of the seven-element array. Similarly, if A_{eff} , η_{pol} , and P_{rec} are known, then the array can reliably be used as a radiometer.

¹ Remember that in a signal processing sense, power is defined as the square of an arbitrary signal. This is distinct from the physical power as seen by the array, which has units of Watts.

Chapter 3

A Two-Stage Receiver for the Focal-Plane Array

3.1 Design Considerations

The primary motivation behind developing a new receiver was the desire to perform experiments in RFI mitigation in conjunction with a phased array feed. Because the prototype array consists of seven elements, the minimum number of receiver channels is also seven. Furthermore, the future plans for the array include an eventual expansion to 19 elements. This means the receivers had to be readily scalable in order to accommodate the addition of more channels.

Because the BYU Very Small Array (VSA) already has four working channels, much of the design for the new receiver was based on the VSA receiver [17]. This helped to greatly simplify the design process because there was no need to redesign a new system from the ground up. It also allowed the revision of the old design to eliminate some of the flaws that were discovered after being put into use.

Like the VSA design, the new receiver is a two-stage frequency translator, but with a few modifications. The most significant modification is a construction out of entirely connectorized components instead of surface-mounts. Cross-talk was a significant problem with the old design, and connectorized components eliminate this by completely encasing the signal in solid coaxial cables. Another major change to the design is a shift in the intermediate frequency from 816 MHz down to 396 MHz. RFI is particularly rampant in the 900 MHz band and this shift makes it much easier to avoid.

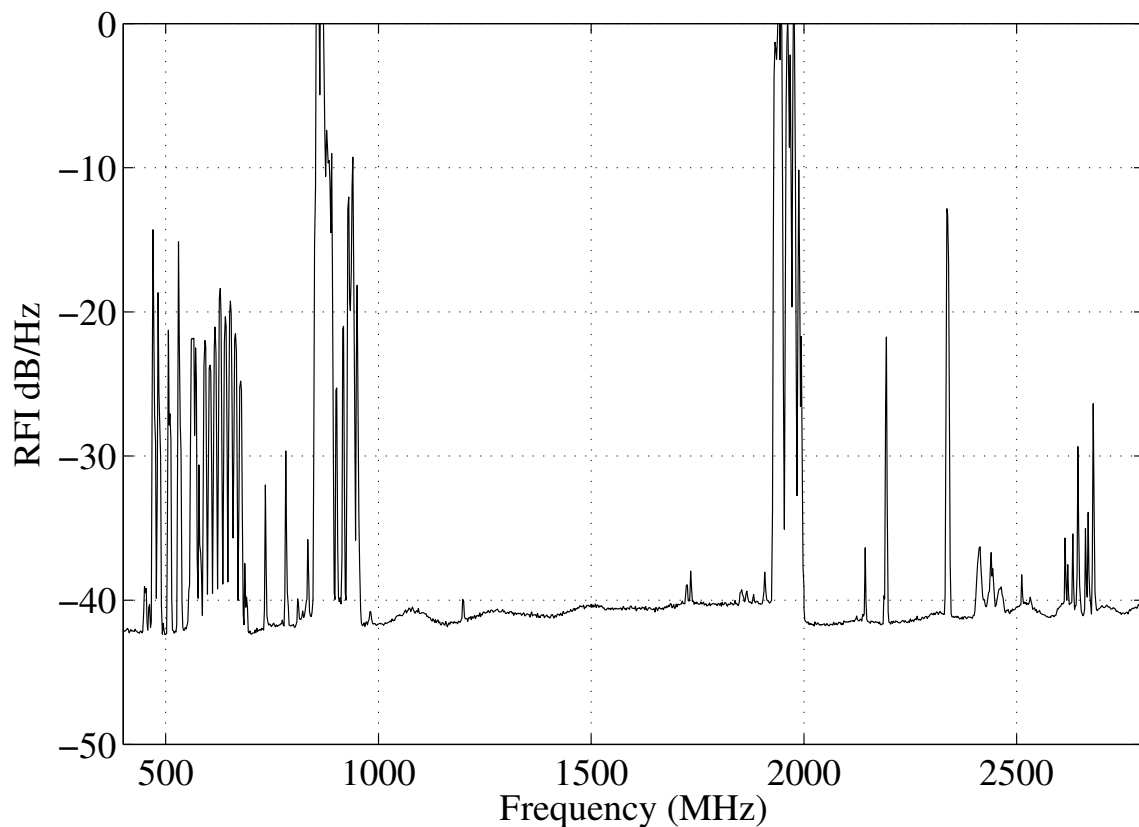


Figure 3.1: RFI survey results. The data was averaged for two minutes on a digital spectrum analyzer.

3.1.1 RFI Survey

Figure 3.1 summarizes the local RFI environment in the Provo-Orem area. The measurement was taken by placing an omnidirectional antenna on the roof of the Clyde building and integrating the signal with a spectrum analyzer. As the figure shows, the protected band from 1400 MHz to 1600 MHz is relatively clear and safe to use in radio astronomy. Note, however, that the image band from 2200 MHz to 2400 MHz has some activity, emphasizing the importance of a good image-rejection filter. Another important band to consider is the range from 800 MHz to 1000 MHz. The VSA design uses an IF frequency at 816 MHz, which is overrun with cellular RFI. Without an exceptional front-end filter, this RFI can bleed through the first-stage

mixer and overlap with the signal of interest. For this reason, it was decided to move the IF frequency on the new receiver from 816 MHz to 396 MHz, where RFI is considerably weaker.

3.1.2 System Overview

An overall block diagram for the new receiver layout is shown in Figure 3.1.2. Note that the system is physically divided into three sections, which will be discussed in detail in their respective chapters. The first is the front-end, which consists of the antenna itself and any devices that must physically rest at the feed. The second is the receiver box, which is a small, aluminum box where the majority of work takes place. The final stage is the back-end, which consists of an anti-aliasing filter, an amplifier, and an analog-to-digital converter.

3.2 Front-End

The front-end of the receiver consists of the antenna, a low-noise amplifier (LNA), and a transmission line. The most important aspect of the front-end is the LNA, which should have a low noise temperature and rest as close to the antenna as possible. For the array feed, the device used is a Mini-Circuits ZEL-1217LN, which has an equivalent noise temperature of about 105 K and a gain of +23 dB.

The final component of the front-end is a transmission line that carries the signal from the feed of the reflector down to the receiver box. Typically, this is accomplished by using standard coaxial cable like RG-217, which is cheap and has low loss. However, RG-217 also has an outer diameter of 0.5 inches, making it relatively rigid. When packed into a bundle of seven, the cables could potentially place too much stress on the reflector. It was therefore decided to employ Hyperlink WCB-200 cable, which has slightly higher loss and is more expensive, but also has an outer diameter of only 0.2 inches. This allows the cable to be more flexible, thereby lowering the stress. The total length of cable is 30 ft, which is just enough to carry the signal from the feed, down along a support strut, around the reflector, and to

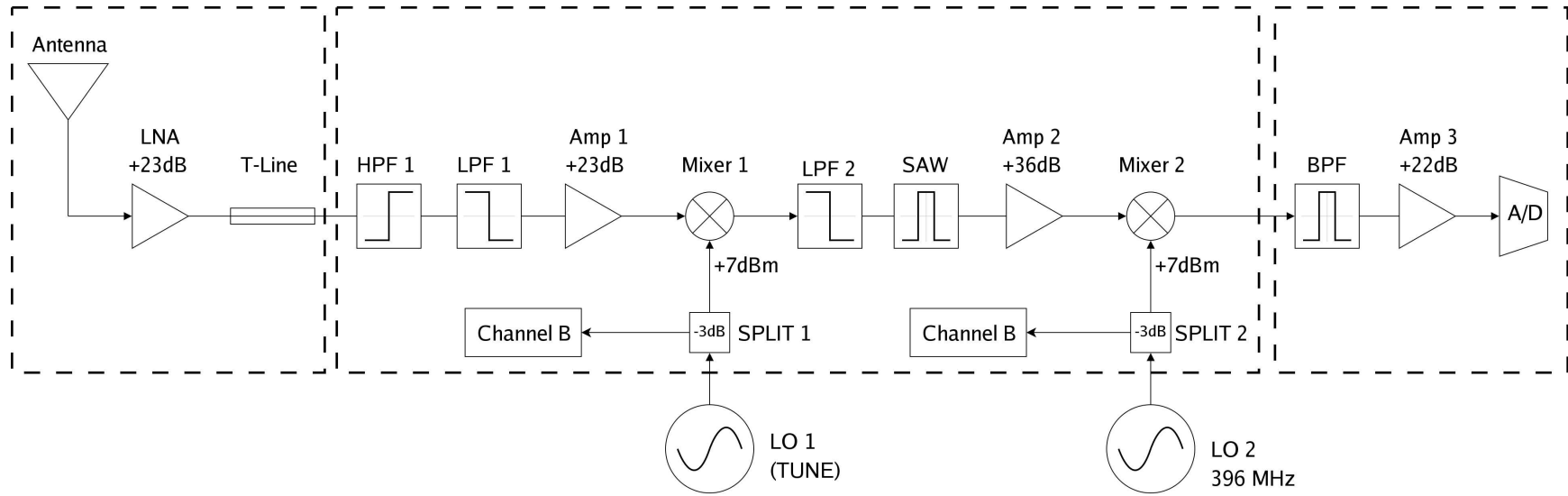


Figure 3.2: Block diagram for the radio astronomy array-feed receivers. The dashed boxes indicate the three major sections.

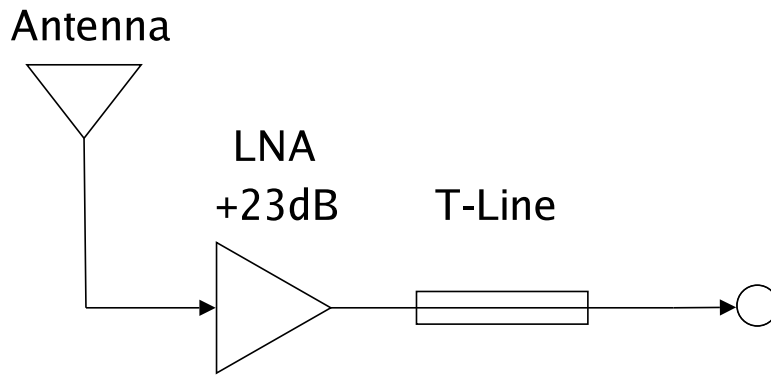


Figure 3.3: Receiver front-end.

receiver boxes on the ground below. The measured loss for a 30 ft length of WCB-200 is 3 dB at 1600 MHz, which is tolerable for the system.

3.3 Receiver Box

To help facilitate scalability, the majority of amplification, filtering, and frequency conversion occurs within a compact, aluminum chassis, called the *receiver box*. A photograph of a receiver box is shown in Figure 3.4 and a block diagram of the inside is shown in Figure 3.5. Each receiver box carries two parallel channels, so four boxes are sufficient to meet the requirement of seven channels. Because each box has two channels, power dividers are employed to split the local oscillator signals among them.

3.3.1 Band-Pass Filter

The first stage in the receiver box is a band-pass filter designed to reject any signals outside of our general range of interest (1400-1700 MHz). Because a single, high quality band-pass filter is difficult to obtain over this frequency range, the filter was constructed by using a series combination of a high-pass filter (HPF1) and a low-pass filter (LPF1). HPF1 is a Mini-Circuits VHF-1200 and LPF1 is a Mini-Circuits VLF-1500. Measured on the network analyzer, a frequency response of the series

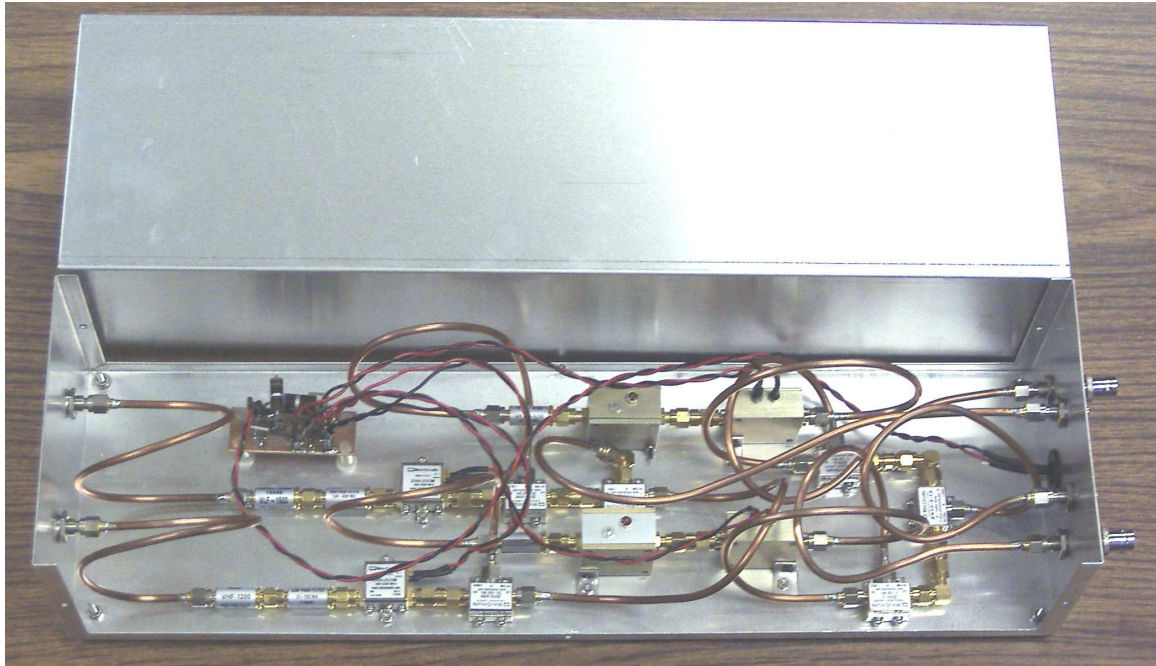


Figure 3.4: Photograph of the receiver box section with the cover removed.

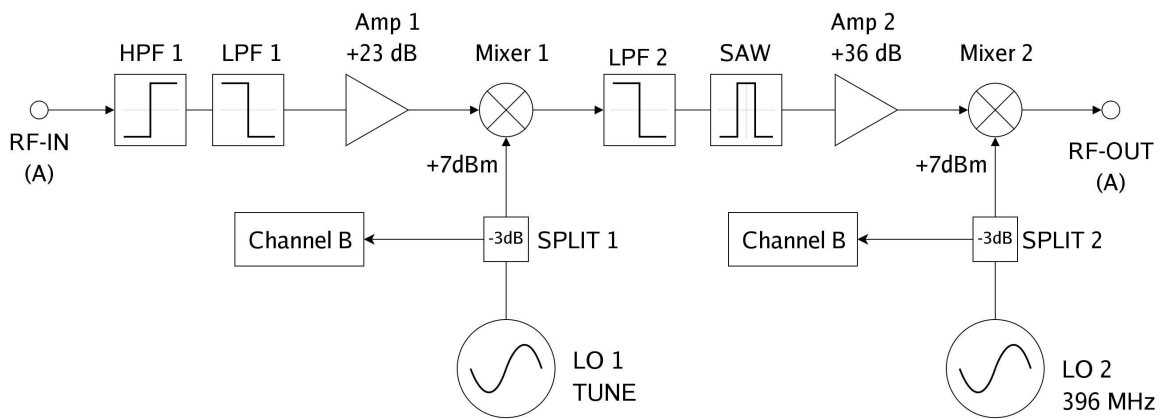


Figure 3.5: Block diagram of the receiver box section. Note that each box contains two channels, labeled A and B.

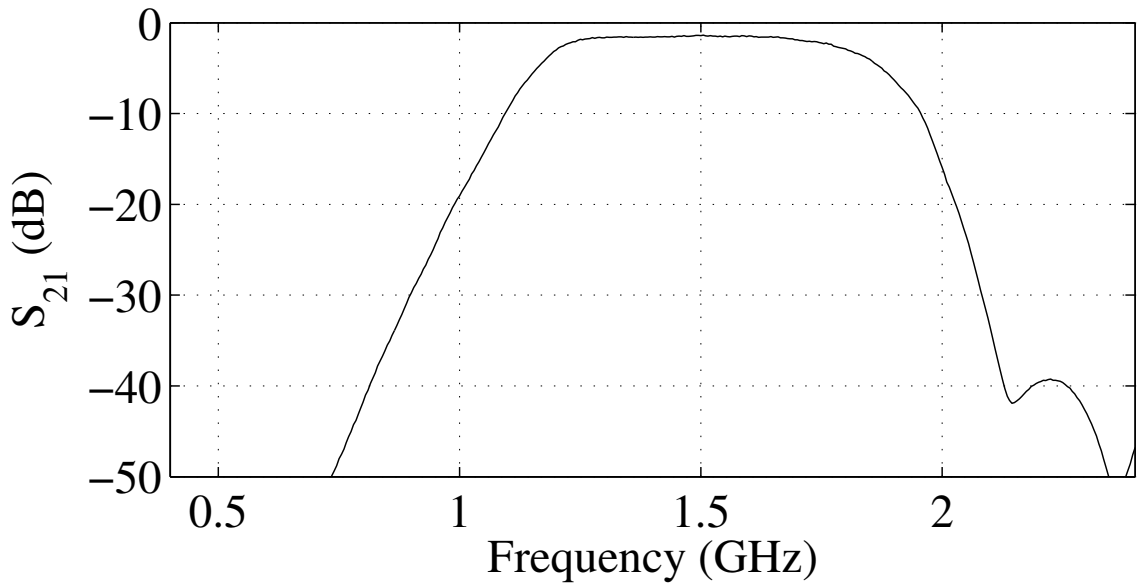


Figure 3.6: Frequency response of the low-pass, high-pass filter combination to form a single band-pass filter.

combination is shown in Figure 3.6. Note that this plot represents the tunable range of frequencies where the receiver box is useful.

The purpose of the initial band-pass filter is twofold. First, it helps to reduce RFI from outside the band of interest. This is especially important around 800 MHz, where RFI is considerably strong. Without the filter, RFI could potentially be strong enough to overdrive the first mixer. The second purpose for the filter is to reject any RFI that lies in the image band of the signal. Without this rejection, the image signal would overlap with the desired signal after passing through the first mixer. For a signal centered at 1600 MHz, the image band is centered at 2400 MHz. As Figure 3.6 shows, the image is rejected by a little over 40 dB.

3.3.2 Amplifier 1 and Mixer 1

The first amplifier in the receiver box is a Mini-Circuits ZX60-2522M and has a gain of 23 dB. It is important to note that the amplifiers are deliberately separated from each other and spaced throughout the receiver. This helps to prevent feedback

oscillations between the amplifiers and avoids overdriving the mixers with too much power.

Mixer 1 is a Mini-Circuits ZX05-30W, and has a conversion loss of 6 dB. Note that the specified LO power level is +7 dBm for this mixer. However, it will still operate well within a range of about +2 dBm to +11 dBm. The trade-off is an increase in conversion loss as the LO power is diminished.

Because the first LO input to the receiver box must power two separate mixers, we must account for the loss due to the power splitter. The first-stage power splitter is a Mini-Circuits ZX10-2-25, which has an insertion loss of 1 dB. Consequently, the total LO input to the receiver box should be +11 dBm. This accounts for a loss of 3 dB from the power division and 1 dB from the insertion loss, leaving +7 dBm to power each mixer.

3.3.3 IF Stage and Mixer 2

The intermediate frequency (IF) stage of the receiver box consists of a low-pass filter (LPF2), a surface-acoustic-wave filter (SAW), and an amplifier (Amp 2). The most important component in the IF stage is the SAW filter, which is a very high-Q bandpass filter. The device used is a Vanlong SF-400, and the frequency response is shown in Figure 3.8. Note, however, that the SF-400 is actually a feed-through device, and not a connectorized SMA device. To connectorize the SAW filters, empty amplifier cases were special-ordered from Mini-Circuits and the SF-400s were soldered to a small piece of micro-strip inside. An example is shown in Figure 3.7.

Although the SAW filter has a very good frequency response around 400 MHz, the response is poor at frequencies above 1000 MHz. Consequently, the bleed-through from the LO input on mixer 1 creates a very strong signal at the output. It is therefore necessary to insert a separate low-pass filter (LPF2) to help supplement the poor high-frequency rejection of the SAW filter. The device used is a Mini-Circuits VLF-530.

The final device in the IF stage is an RF Bay LPA-6-26 amplifier with 36 dB of gain, which feeds the signal to mixer 2. Like mixer 1, mixer 2 is fed by a single LO that is split among the two channels. The second power splitter (SPLIT 2) is a

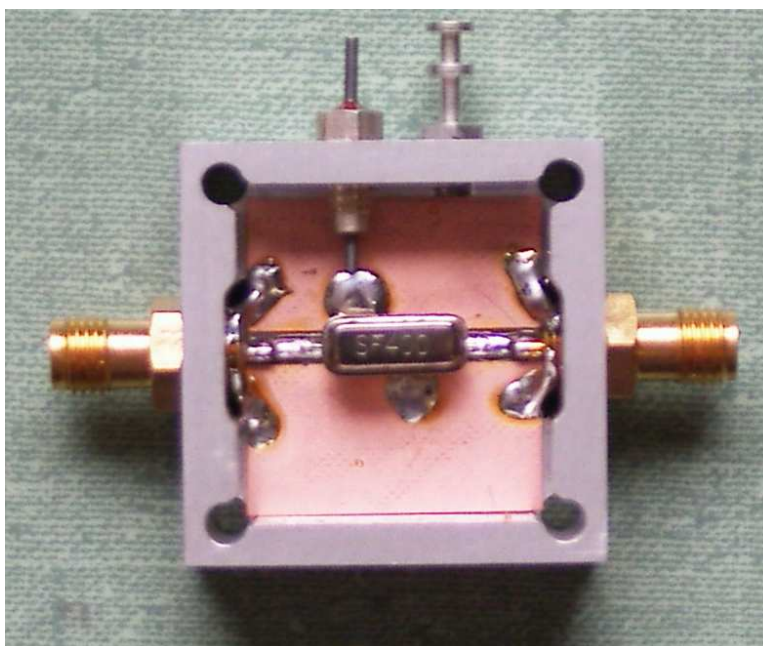


Figure 3.7: SAW filter soldered into the a Mini-Circuits amplifier case. The SAW is a passive device, so the power leads are left floating.

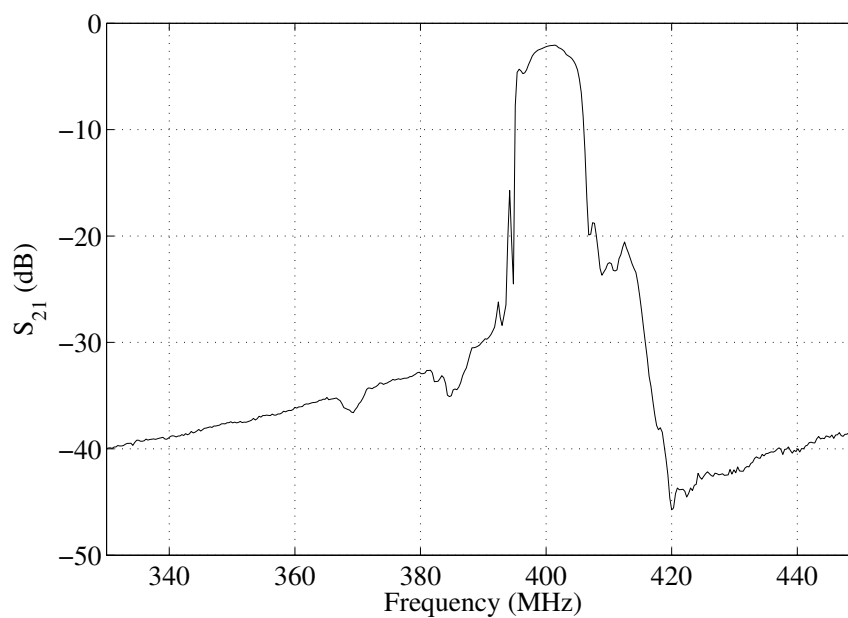


Figure 3.8: Frequency response of the SAW filter.

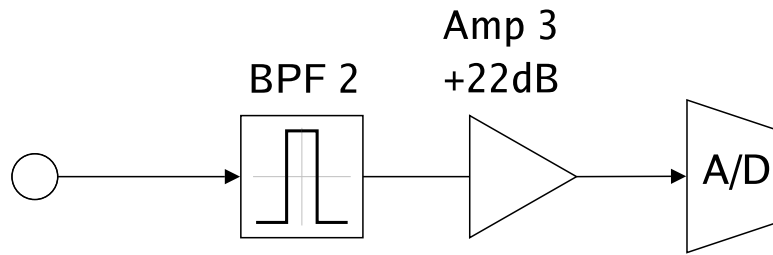


Figure 3.9: Receiver back-end.

Mini-Circuits ZX10-2-12, and has similar insertion loss to SPLIT 1. Thus, the second LO input requires an input power of +11 dBm in order for mixer 2 to receive +7 dBm on both channels.

3.4 Back-End

The final stage of the receiver is the back-end, which consists of an anti-aliasing filter (BPF 2), an amplifier (Amp 3), and an analog-to-digital converter (A/D). The device used for BPF 2 is a customizable filter with a passband determined by the sampling rate from the A/D. At present, the maximum practical sampling rate for eight channels is 2.5 MS/s, giving a Nyquist frequency of 1.25 MHz. The filter bandwidth is therefore padded slightly below this value to 1.05 MHz. It is important to note, however, that the center frequency of BPF 2 is chosen to lie at 3.125 MHz. This places the filter bandwidth in the center of the second Nyquist zone, which ranges from 2.5 - 3.75 MHz. In other words, the final signal is deliberately aliased through a process called *baseband subsampling*. The reason for this design is the SAW filter, which has about 2 MHz of roll-off from the passband to the stopband. Baseband subsampling allows looser constraints on the anti-aliasing filter without giving up any information in the signal.

In practice, high bandwidth may not always be a priority. For testing purposes, it is convenient to employ a sampling rate of 1.25 MHz because it reduces the amount of data to process. This requires a new set of anti-aliasing filters to be

installed at the back-end. To accommodate this sort of situation, the back-end has been designed to allow easy replacement of the anti-aliasing filters.

The final amplifier in the system is a Mini-Circuits ZFL-500 which has 22 dB of gain. This device provides the final boost in signal strength before it is sampled by the A/D, which is a National Instruments PCI-6115 resting inside of a desktop computer.

3.5 DC Power

A minor complication arises with the receiver box because Amp 1 requires an input voltage of +5 V while Amp 2 requires +12 V. Furthermore, it is sloppy to feed these amplifiers directly with DC voltage, since the necessarily long wires would tend to introduce ground loops. To mitigate this issue, each receiver box is equipped with its own voltage regulation to power the amplifiers. Figure 3.10 shows a schematic of the voltage regulation circuit. The 12 V converter is an LM340T12 and the 5 V converter is an LM340T5. These regulators are powered by direct inputs of 15 V and 12 V respectively from an external DC supply. To help keep voltage ripple to a minimum, the standard practice is to install shunt capacitors at the input and output of each voltage regulator.

3.6 Summary and Characterization

A summary of the important devices in the receiver is shown in Table 3.2, which also includes a summary of the gains and losses for each device. Table 3.3 lists the minor components, such as connectors and adapters, that are necessary for connecting the major devices together. Table 3.1 summarizes many of the important characteristics of the receiver box section. For convenience, an explanation of the terms is provided below.

1. *Cost*: Approximate dollar amount per channel for the receivers.
2. *Net Gain*: Net power gain for a channel. This value can vary slightly with frequency, temperature, etc, on the order of ± 1.0 dB

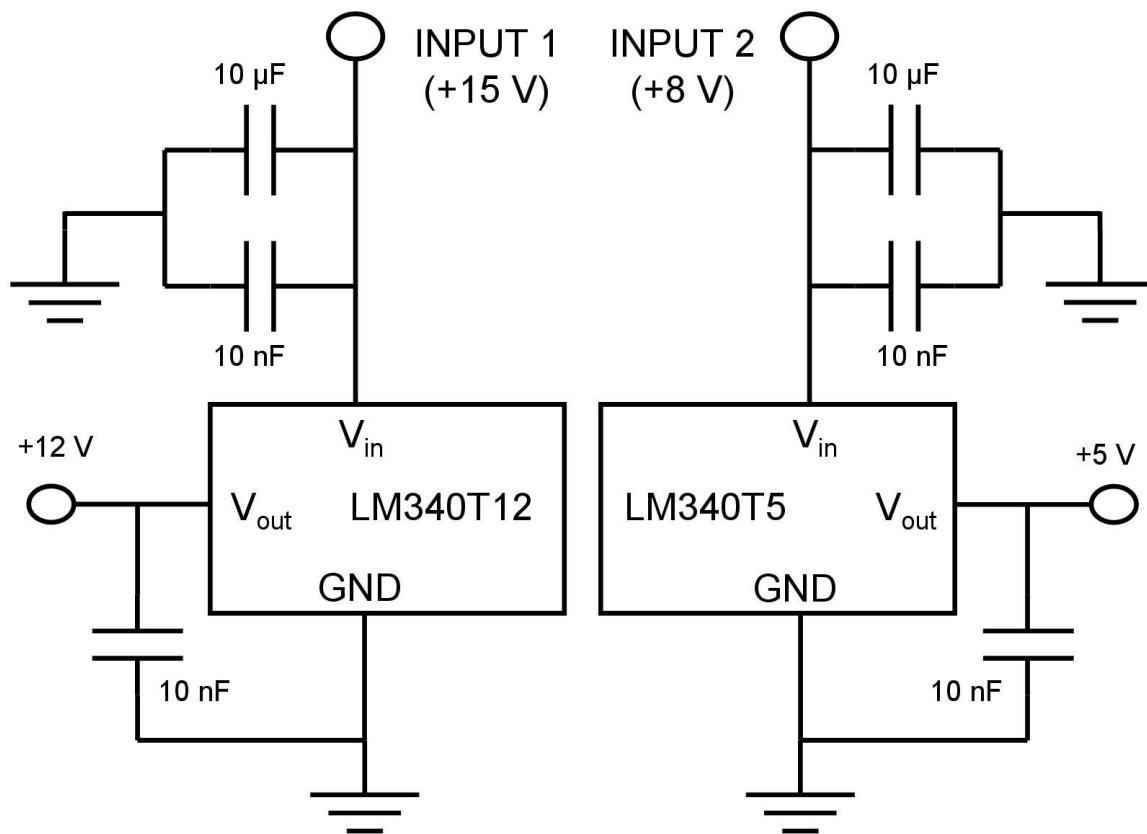


Figure 3.10: DC-DC regulator configuration.

3. *Noise Temperature*: Equivalent noise temperature of a receiver channel, measured by using the standard Y-factor method [22].
4. *Input Frequency Range*: Frequency range where the input filters have the least attenuation. The receiver is still useful beyond this range, but the filters will either attenuate the signal or sacrifice image rejection.
5. *Image Rejection*: Attenuation of the image band over the input frequency range. With high-side mixing and an IF of 400 MHz, the image band is centered at the signal band plus 800 MHz.
6. *Cross Talk*: A measure of attenuation on a signal input to channel A that exits from channel B. This is due to the RF/LO bleedthrough at the mixers and

the imperfect isolation of the power dividers. It is strongest between adjacent channels in the same box. Between separate boxes, the cross-talk depends strongly on the quality of isolation between the LO inputs.

7. *Harmonic Distortion*: This is a measure of how far the first nonlinear harmonic lies below the signal of interest.
8. *LO Input Range*: Range of LO powers where the receiver still performs reasonably well. The mixers in the receiver will function normally even if the LO power is below spec, but the trade-off is a small increase in conversion loss. However, the conversion loss becomes increasingly pronounced as the mixers receive +2 dBm or less. If the LO power is too high, then the mixers experience a high risk of failure and may require replacement.
9. *Nominal LO Power*: Ideal LO input power to the receivers. This accounts for the power splitter losses to ensure that each mixer receives their specified +7 dBm. Note that this is the same for both the tunable LO and the intermediate LO.

Table 3.1: Receiver characterization.

Cost	\approx \$ 1045.00
Net Gain	+80 dB
Noise Temperature	120 K
Input Frequency Range	1400-1700 MHz
Image Rejection	-41 dB
Cross Talk	-51 dB
Harmonic Distortion	-58 dB
LO Power Range	6-15 dBm
Nominal LO Power	+11 dBm
LO 1 Frequency	1800-2200 MHz
LO 2 Frequency	396 MHz

Table 3.2: Major parts list and power budget.

Part Name	Part Number	Manufacturer	Unit Price (\$)	Gain (dB)
LNA	ZEL-1217LN	Mini-Circuits	274.95	+23
T-Line	WCB-200	Hyperlink	49.00	-3.0
HPF1	VHF-1200	Mini-Circuits	19.95	-0.5
LPF1	VLF-1500	Mini-Circuits	19.95	-1.0
AMP1	ZX60-2522M	Mini-Circuits	59.95	+23
Mixer 1	ZX05-30W	Mini-Circuits	37.95	-6.0
LPF2	VLF-530	Mini-Circuits	19.95	-0.5
SAW	SF400	Vanlong	22.88	-3.0
AMP2	LPA-6-26	RF Bay	99.99	+36
Mixer 2	ZX05-2	Mini-Circuits	37.95	-6.0
BPF	FN-3521	Filtronetics	210.00	-2.0
AMP3	ZFL-500	Mini-Circuits	69.95	+22
SPLIT 1	ZX10-2-25	Mini-Circuits	24.95	-4.0
SPLIT 2	ZX10-2-12	Mini-Circuits	24.95	-4.0

Table 3.3: Minor parts list.

Description	Part Number	Vendor	Unit Price (\$)
SMA Male-Male	161293	Jameco	2.95
SMA Male-Male Panel Mount	160012	Jameco	3.99
SMA Male-Female, Rt Angle	161306	Jameco	4.49
SMA Male to BNC Female	159476	Jameco	2.69
SMA Male to BNC Male	153592	Jameco	2.69
RG402 Semi-Rigid Coax (1 ft)	RG402/U	Pasternack	2.90
SMA Connector to RG402 Cable	ARF1185-ND	Digikey	3.91
Conxall Mini Con-X Cable Pin	6282-3PG-3XX	Digikey	4.44
Conxall Mini Con-X Chassis Mount	7282-3SG-300	Digikey	5.45
Aluminum Chassis	TF-788	Action Electronics	26.59

Chapter 4

The Seven-Element Hexagonal Array

4.1 Array Geometry

The prototype array feed, depicted in Figures 4.1 - 4.4, was modeled after the simulations performed in [16] and consists of seven dipole antennas arranged in a hexagonal grid over a ground-plane backing. Because the L-band is popular for radio astronomy research, the array elements were designed for a center frequency of 1600 MHz which corresponds to a wavelength of $\lambda = 18.75$ cm. The element spacing was fixed at 0.6λ (11.25 cm), which is small enough to fully sample the incoming electric fields and also large enough to significantly reduce the effects of mutual coupling [23].

The ground plane of the array was constructed out of 1.5 mm copper-clad laminate. To add extra support, a ring of Plexiglas was attached along the bottom edge of the ground plane. Four steel standoffs were bolted to the bottom of the array, allowing it to be attached to the support struts of a 3-meter reflector. This required the struts to be bent slightly, and Antenna 1 on the 5th-floor roof of the Clyde Building is the only reflector that has been modified to accept the array.

4.2 Element Characterization

Each array element, shown in Figure 4.2, is a standard balun-fed dipole at a distance of 0.25λ (4.7 cm) above the ground plane [24]. The coaxial feed to the dipole was made with RG402 semi-rigid cable, which has an outer diameter of 3.4 mm. The balun was constructed by stripping a section of copper shielding from the semi-rigid cable and soldering it adjacently to the feed at a distance of 4 mm. The



Figure 4.1: Photograph of the prototype array feed.

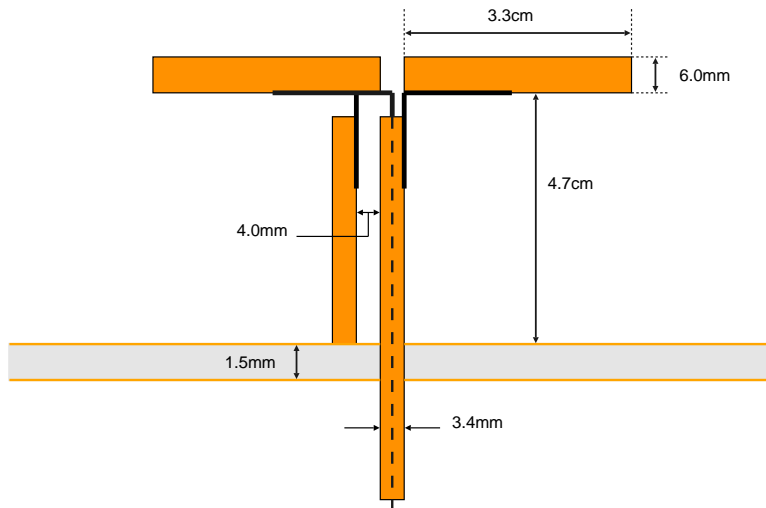


Figure 4.2: Diagram of an array element. Each element is a balun-fed dipole with a ground-plane backing.

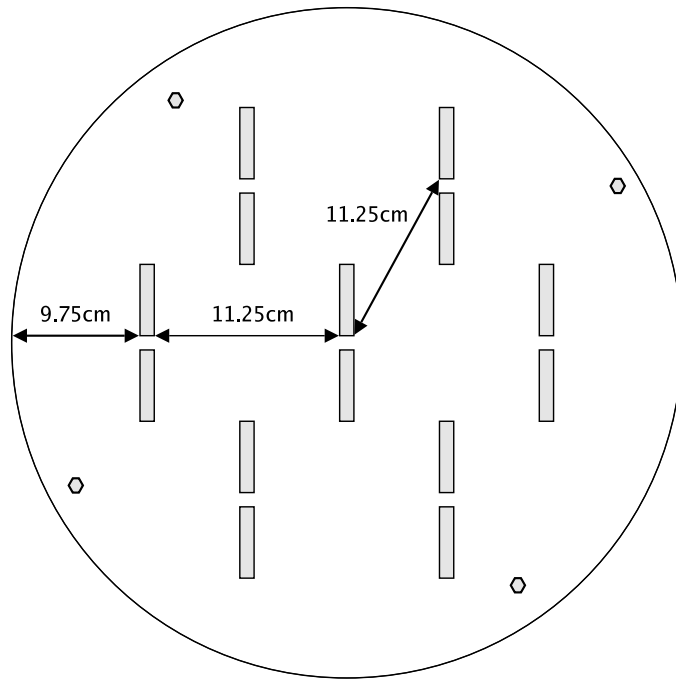


Figure 4.3: Top schematic of the prototype array.

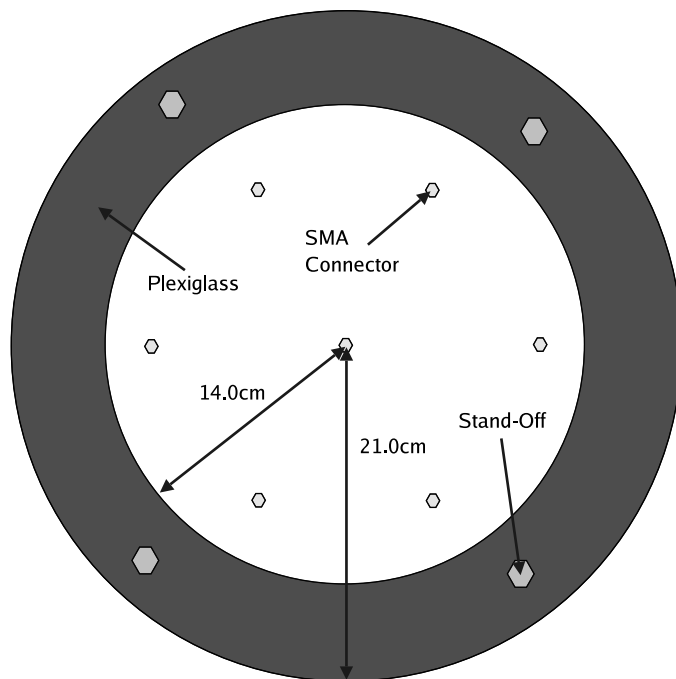


Figure 4.4: Bottom schematic of the prototype array.

arms of the dipole were made out of 6.0 mm copper pipe, with a radius-to-wavelength ratio of $a/\lambda = 0.016$. Note that this is relatively thick for dipole arms, which causes increased bandwidth and lowered self impedance.

4.2.1 Self Impedance

The self impedance Z_S of an antenna element is related to the voltage reflection coefficient Γ by

$$Z_S = Z_0 \frac{1 + \Gamma}{1 - \Gamma} \quad (4.1)$$

where $Z_0 = 50 \Omega$ is the characteristic impedance of the transmission line feeding the element. Figure 4.5 shows the self impedance of each antenna element. These values were calculated by using a network analyzer to measure the input reflection coefficient as a function of frequency. Note how the impedance near 1600 MHz is very close to 50Ω , so there is little need to include a matching network with each antenna.

4.2.2 Bandwidth

Although a strict definition of antenna bandwidth is somewhat arbitrary, a common definition uses the range of frequencies with a reflection coefficient less than -10 dB. The center frequency f_0 is defined as the frequency with the minimum reflection coefficient, or equivalently, the frequency where the antenna is most closely matched to the characteristic impedance of the transmission line. The *percent bandwidth* B_0 is then defined as the ratio of the total bandwidth to the center frequency,

$$B_0 = \frac{f_u - f_l}{f_0} \quad (4.2)$$

where f_u and f_l are the upper and lower intercepts at -10 dB. Figure 4.6 shows the reflection coefficients of the individual antenna elements when measured on a network analyzer. Using these measurements, the average antenna bandwidth of the array was found to be 32 percent, with good frequency coverage from 1.5GHz - 2.0GHz.

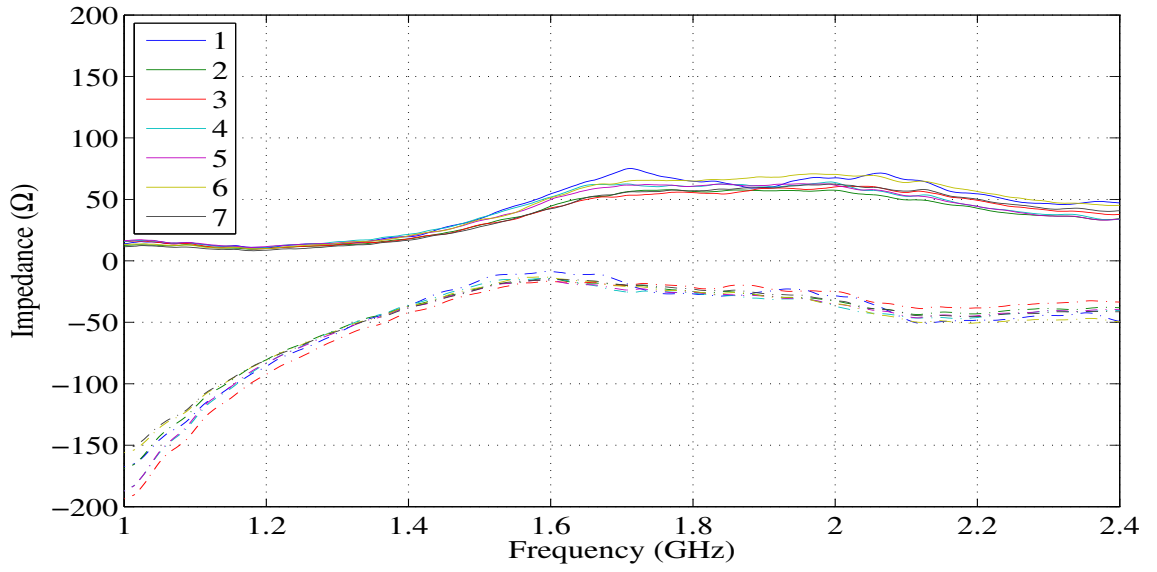


Figure 4.5: Self impedances of the array elements. The solid lines indicate real impedance while the dashed lines indicate imaginary impedance.

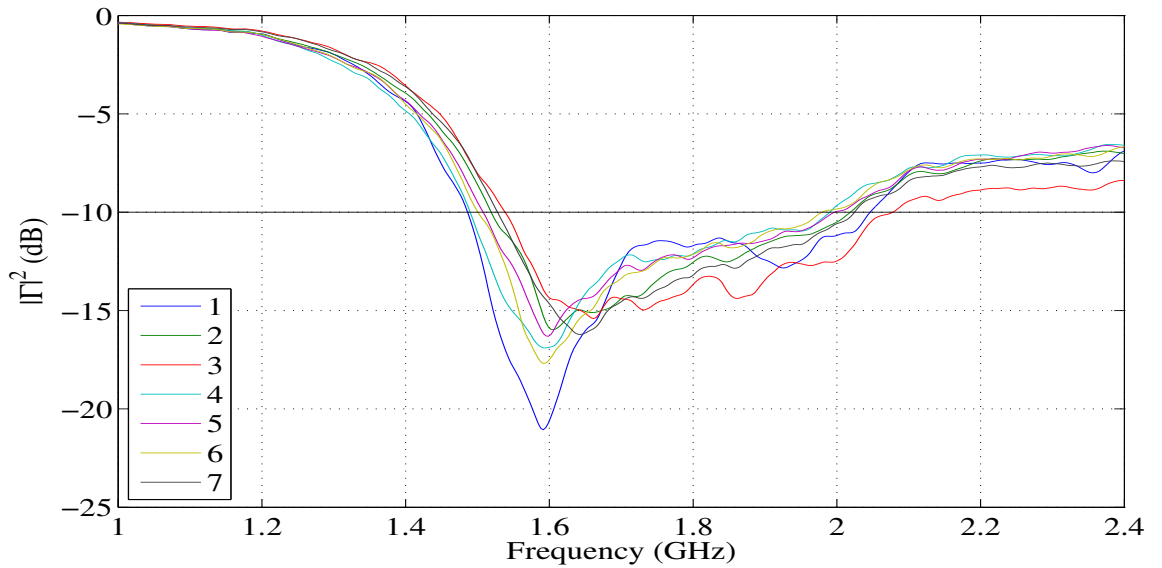


Figure 4.6: Measured reflection coefficients of the 7-element array. The average center frequency is 1.61GHz, with an average reflection coefficient magnitude of -17 dB.

4.3 Mutual Coupling

Mutual coupling between dipole elements has the potential to adversely affect array performance [25]. It was quantified by treating the array as a 7-port microwave network and then measuring the transmission coefficients with a network analyzer. The results for this measurement are shown in Figure 4.7. Note that for each measurement between two elements, the other five were terminated with open-circuit loads.

From the geometry of the array, there are six unique arrangements between any pair of elements $[m, n]$. Each of these arrangements can be described by the horizontal and vertical offsets (x, y) between dipoles. Note that certain arrangements have repeated symmetry between several elements. For example, we can expect the mutual coupling between elements $[1, 2]$ to closely resemble that between elements $[5, 1]$, since they both share the same offset of $(0.6d, 0)$. The length d is defined as 18.75 cm, which is one unit of wavelength at 1600 MHz. A summary of the arrangements is provided below:

1. $(x, y) = (0.6d, 0)$, shared by elements $[2, 1]$, $[5, 1]$, $[4, 3]$, and $[7, 6]$.
2. $(x, y) = (0.3d, \sqrt{0.27}d)$, shared by elements $[3, 1]$, $[4, 1]$, $[6, 1]$, $[7, 1]$, $[3, 2]$, $[7, 2]$, $[5, 4]$, and $[6, 5]$.
3. $(x, y) = (0.9d, \sqrt{0.27}d)$, shared by elements $[4, 2]$, $[6, 2]$, $[5, 3]$, and $[7, 5]$.
4. $(x, y) = (0.6d, 2\sqrt{0.27}d)$, shared by elements $[6, 3]$, and $[7, 4]$.
5. $(x, y) = (0, 2\sqrt{0.27}d)$, shared by elements $[7, 3]$ and $[6, 4]$.
6. $(x, y) = (1.2d, 0)$, shared by elements $[5, 2]$.

4.4 Gain and Effective Area

Recall from Section 2.5 that effective area is defined as

$$A_{eff} = \frac{P_{rec}}{\eta_{pol} S_{inc}} \quad (4.3)$$

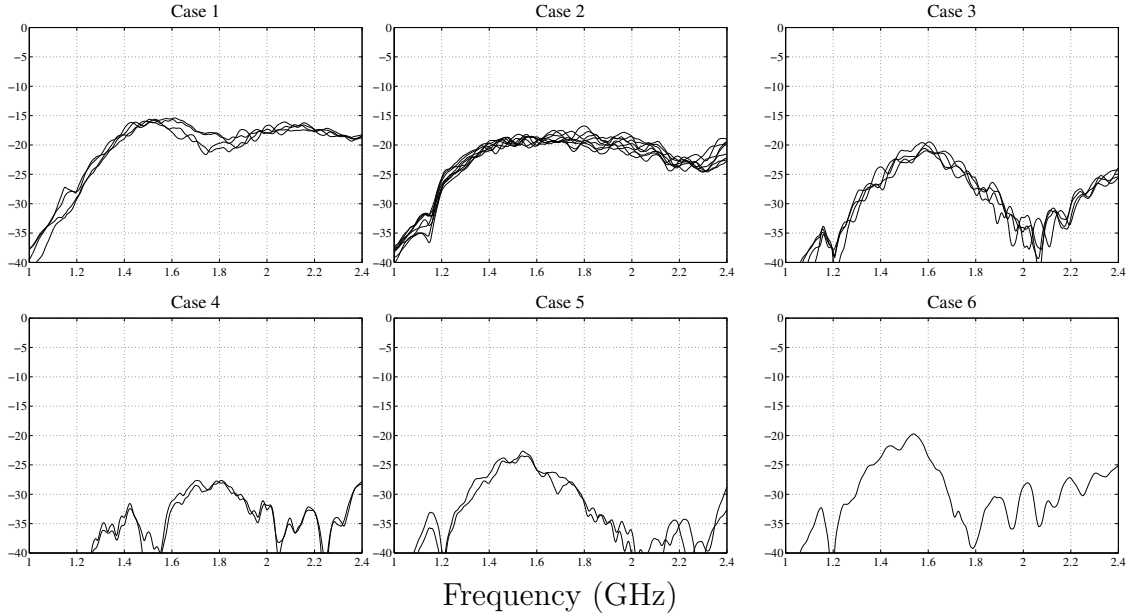


Figure 4.7: Transmission coefficient $|S_{21}|^2$ in dB for the six mutual coupling cases.

where S_{inc} is the power density of an incident plane wave, η_{pol} is the polarization efficiency of the array, and P_{rec} is the total power received by the array. A closely related quantity is the receive gain G_r of the array, which is proportional to the effective area through the relation

$$G_r = \frac{4\pi A_{eff}}{\lambda^2} . \quad (4.4)$$

The boresight gain of the array was measured by using the two towers on the 5th-floor roof of the Clyde Building. Shown in Figure 5.1, the experimental setup consisted of two 20 ft towers separated by a distance of 50 ft. A horn antenna sat atop the north tower and transmitted a CW signal. Directly facing the horn was the array feed, which sat on the south tower. The array was aligned in polarization with the transmit horn, so a value of $\eta_{pol} = 1$ can be assumed.

To calculate S_{inc} , a link budget was traced back to the signal generator that originally produced the signal. For a total radiated power of P_{rad} from the horn

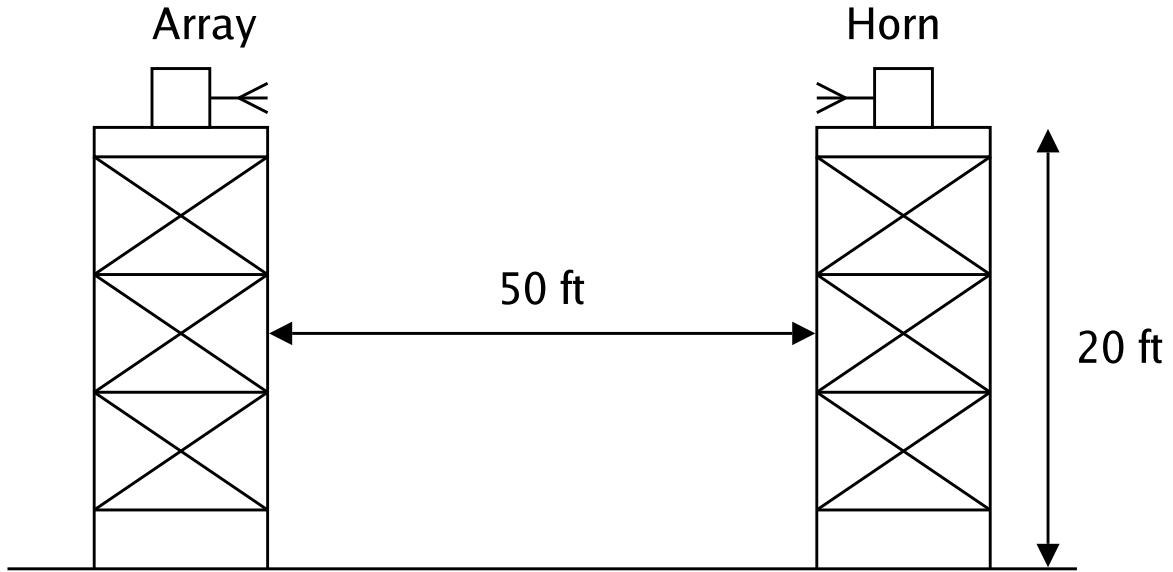


Figure 4.8: Experimental setup on the roof of the Clyde building used to measure the boresight gain of the 7-element array.

antenna, the power density incident on the array is given by

$$S_{inc} = \frac{G_t P_{rad}}{4\pi r^2} \quad (4.5)$$

where $r = 50$ ft is the distance between the towers and G_t is the gain of the transmitting antenna. The antenna used as a transmitter was a Scientific Atlanta standard gain horn model 12-1.7, which has a gain of 14.0 dBi at 1600 MHz. To calculate P_{rad} , it was necessary to account for the line loss from the signal generator to the horn antenna, which was measured to be 5.4 dB at 1600 MHz. Also, one must account for the impedance mismatch between the horn antenna and the transmission line. Measured on a network analyzer, this introduced another 0.7 dB of loss. Thus, for a total generated power of -85 dBm, P_{rad} is found to be -91 dBm and S_{inc} is calculated at 6.6×10^{-15} W/m².

The beamformer used to combine the array elements was an adaptive version of LCMV,

$$\mathbf{w} = \mathbf{R}_{xx}^{-1} \mathbf{d}_s \quad (4.6)$$

where the array weight vector \mathbf{w} was recalculated for every 2.5 ms of data and the signal steering vector \mathbf{d}_s was calculated from training data. The total power received by the array was then calculated using Equation 2.43, rewritten here as

$$P_{rec} = \frac{1}{\alpha_1 \alpha_2} \mathbf{w}^H \mathbf{R}_{ss} \mathbf{w} \quad (4.7)$$

where the constant α_1 is given as

$$\alpha_1 = \frac{|g_r|^2 |Z_0|^2}{R_{rad}} \quad (4.8)$$

and α_2 is given as

$$\alpha_2 = \mathbf{w}^H \mathbf{A} \mathbf{w} . \quad (4.9)$$

From the results in Section 4.2.1, the self-impedance R_{rad} of each antenna element is approximately 50Ω , as well as the characteristic impedance Z_0 . The gain g_r of each receiver channel was calibrated by feeding a known, -110 dBm signal to each input and observing the total power at the each output¹. The pattern overlap matrix \mathbf{A} , however, is difficult to measure in practice. Fortunately, \mathbf{A} is a diagonally dominant matrix whose main diagonal is identically all 1's. This means the identity matrix \mathbf{I} is a close approximation to \mathbf{A} , and has been observed to introduce an uncertainty on the order of 0.5 dB or less. A close approximation to α_2 is therefore given by setting $\mathbf{A} = \mathbf{I}$, resulting in

$$\alpha_2 \approx \mathbf{w}^H \mathbf{w} . \quad (4.10)$$

Using these values, the final power output power seen by the antenna array was calculated at -124 dBm. This gives a total boresight gain of 13 dBi and an effective area of 550 cm^2 . A good theoretical comparison is the Hertzian dipole model from Section 2.1.2. Applying this model results in a total boresight gain of 12 dBi, which compares fairly well to the measured value.

¹ Note that because the gain of each receiver channel is slightly different, Equation 4.8 had to be slightly modified so that g_r is a vector that acts on each channel individually, rather than a single scalar that acts on every channel at once.

Chapter 5

Antenna Test Range Receiver Design for the NRAO Headquarters

At the headquarters for the National Radio Astronomy Observatory (NRAO) in Green Bank, West Virginia, there resides a twin-tower antenna test range. Currently, the test range is capable of producing accurate cut patterns for single element antennas, but there is a desire to upgrade the range with the capability to measure cut patterns for entire antenna arrays. This chapter presents the details of a receiver design that is intended to replace the current system in use. To prove the design, the seven-element prototype array was used as a test platform to demonstrate the measurement of several cut patterns of array directivity.

Note that at the time of this writing, the design had not been finalized with specific devices, but a demonstration had been performed with a prototype receiver constructed out of spare parts. In the future, it will be important to catalog the final devices and perform a robust characterization. There is also a great deal of work to be done with the automation of the platform and post-processing of the data.

5.1 Geometry

The basic geometry of the range, shown in Figure 5.1, consists of two 35 ft towers that are separated by a distance of 48 ft. The transmitter tower holds a horn antenna (Tx) that beams energy across the range to the antenna under test (AUT). On top of the receiver tower lies a turret which spins the AUT in azimuth. As the turret spins, the electric field at the AUT is sampled over a specified range of angles, providing a cut measurement of antenna gain.

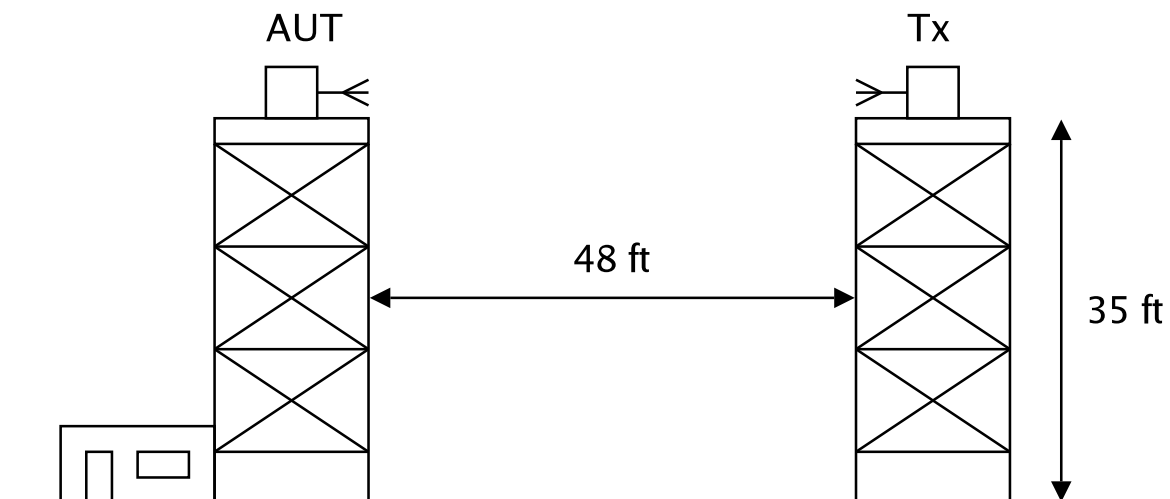


Figure 5.1: Geometry for the antenna test range. The AUT sits on top of a rotating turret, which allows the measurement of antenna gain.

The controls for the antenna range lie inside a small shack adjacent to the receive tower, with long lines of coaxial cable connecting to the Tx and the AUT. In order to measure a voltage phasor from the AUT, a receiver is required to translate the high frequency signals down to baseband. Although a functional receiver is already in use, the current system is relatively outdated and can only measure gain for a single antenna. During the summer of 2005, the receiver was redesigned as part of an upgrade to allow automated gain measurements of antenna arrays.

5.2 The Lock-In Amplifier

The most important device in the receiver is the lock-in amplifier (LIA). At its core, the LIA is basically just a device that can take very precise measurements of amplitude and phase on continuous wave (CW) signal. The specific device used in the NRAO receiver is the Stanford Research Systems model SR830. A full product description can be found online¹, but the most important aspects will be provided in this chapter.

¹ <http://www.srsys.com/products/SR810830.htm>

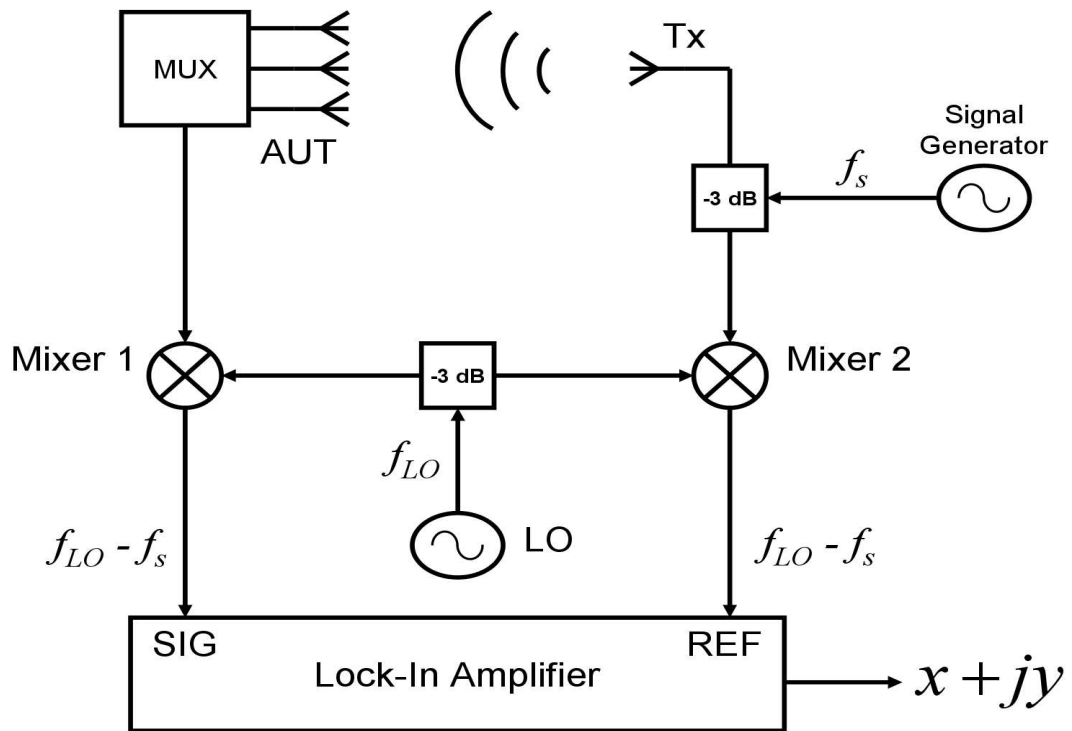


Figure 5.2: Concept design for the single-stage lock-in receiver.

The LIA has two input channels, labeled *reference* (REF) and *signal* (SIG). The REF input is a pure CW signal that tells the LIA which frequency to “lock in” to. Once locked in, the LIA reads the SIG input and singles out any signal at the same frequency as the reference. It then returns a complex number that represents the phaser of the signal of interest (SOI). Because the LIA can single out a very narrow bandwidth, it is capable of detecting extremely weak signals with a very high precision.

In order to “lock in” to the REF signal, the LIA requires a stable sinusoid with a minimum strength of $400\text{mV}_{\text{pk-pk}}$. The input impedance to the REF channel is $1.0\text{ M}\Omega$, and the usable frequency range for measuring signals is $1.0\text{mHz} - 102\text{kHz}$.

5.3 Theoretical Design Layout

Shown in Figure 5.2, the basic concept behind the antenna range receiver is a dual, single-stage frequency translator. The system begins with a signal generator that produces a CW signal at frequency f_s which is then separated into two distinct signals by a power splitter. One of these signals is mixed directly down to baseband where it is sent to the REF channel of the LIA and serves as the reference. The second signal is transmitted across the antenna range where it is received by the AUT and then also mixed down to baseband. After mixing, the signal is fed to the SIG channel of the lock-in amplifier, where it is measured as a voltage phasor ($x + jy$). As the turret rotates, the phasor will vary in response to the directivity of the AUT. To switch between antenna elements, a manifold of digitally controlled switches (MUX) rests between the antenna array and the receiver.

5.4 LO Frequency

The final frequency at baseband is somewhat arbitrary, limited only by the precision of the signal generators and the bandwidth of the LIA. In practice however, it is sensible to keep the local oscillator frequency f_{LO} as far from f_s as possible. It is therefore preferable to set the baseband frequency toward the maximum limit of the LIA,

$$|f_{LO} - f_s| = 100 \text{ kHz} . \quad (5.1)$$

Since the signal frequency f_s is a variable that changes with the specifications of the AUT, f_{LO} can be expressed as a function of f_s ,

$$f_{LO} = f_s \pm 100 \text{ kHz} . \quad (5.2)$$

Note that it matters very little which LO frequency is chosen, since the baseband frequency will be the same in either the plus or minus case.

5.5 Power Losses

The diagram in Figure 5.2 is merely a concept design and does not take into account the non-ideal nature of the parts in a real system. In order to understand

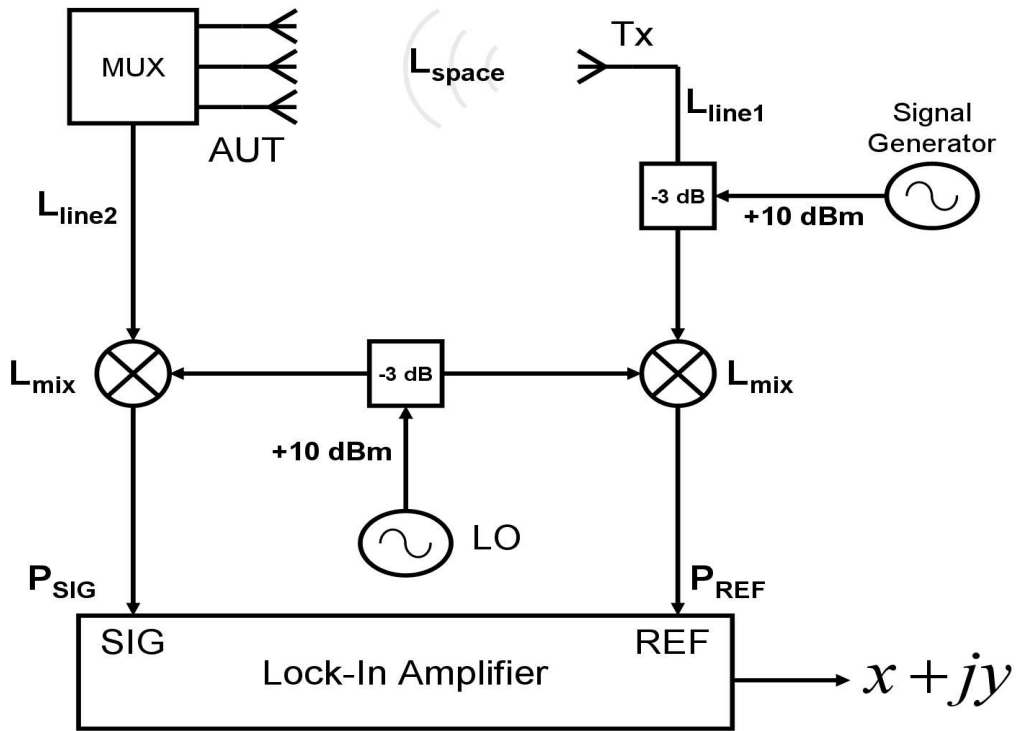


Figure 5.3: Revised diagram indicating the major power losses.

the required changes for a practical receiver, it was helpful to first analyze the power losses. The diagram in figure 5.3 presents a model of the major power losses in the system. Under this model, there are four significant sources of power loss: Line loss (L_{line}), space-propagation loss (L_{space}), mixer conversion loss (L_{mix}), and power-splitter loss (-3 dB).

5.5.1 Line Loss

The line losses in the system are a function of the transmission lines used to carry signals. The system currently uses RG-213 coaxial cable, which is rated at 1600 MHz for a loss of 10 dB per 100 feet of cable. Using the geometry of the antenna towers, the line losses are calculated as $L_{line1} = -8.3$ dB and $L_{line2} = -3.5$ dB. To be conservative, these values should be rounded to -10 dB and -5 dB, respectively.

5.5.2 Propagation Loss

The free-space propagation loss is given by the Friis equation,

$$L_{space} = G_t G_r \left(\frac{\lambda}{4\pi r} \right)^2 \quad (5.3)$$

where G_r is the AUT gain, G_t is Tx gain, and $r = 48$ ft is the distance between the towers, and $\lambda = 0.1875$ m is the operational wavelength for the array feed. The value of G_t can vary depending on the type of antenna used, but in practice it is common to employ a horn antenna on the order of $G_t = 10$ dB (the actual value will vary with frequency). Note that G_r has no distinct value, since it is a variable that will change with AUT rotation. It is therefore useful to fix $G_r = 1$ and instead consider it in terms of the dynamic range of the receiver. Using these values, the propagation loss is on the order of $L_{space} \approx -50$ dB.

5.5.3 Conversion Loss

Conversion loss is encountered whenever a signal is translated in frequency by a mixer. For a typical commercial mixer, the conversion loss is on the order of 7 dB.

5.5.4 Splitter Loss

The power splitter losses are simply the result of dividing a signal from one transmission line into two, thus cutting the total power in half. For a standard Wilkinson power divider, the loss from power splitting is fixed at -3 dB, plus a negligible amount of insertion loss.

5.5.5 Power Budget

The maximum transmit power available from most signal generators is about +10 dBm. Using the estimated loss values, it is a simple matter to calculate the signal and reference powers to be on the order of

$$P_{SIG} \approx -65 \text{ dBm} \quad \text{and}$$

$$P_{REF} \approx -3 \text{ dBm} .$$

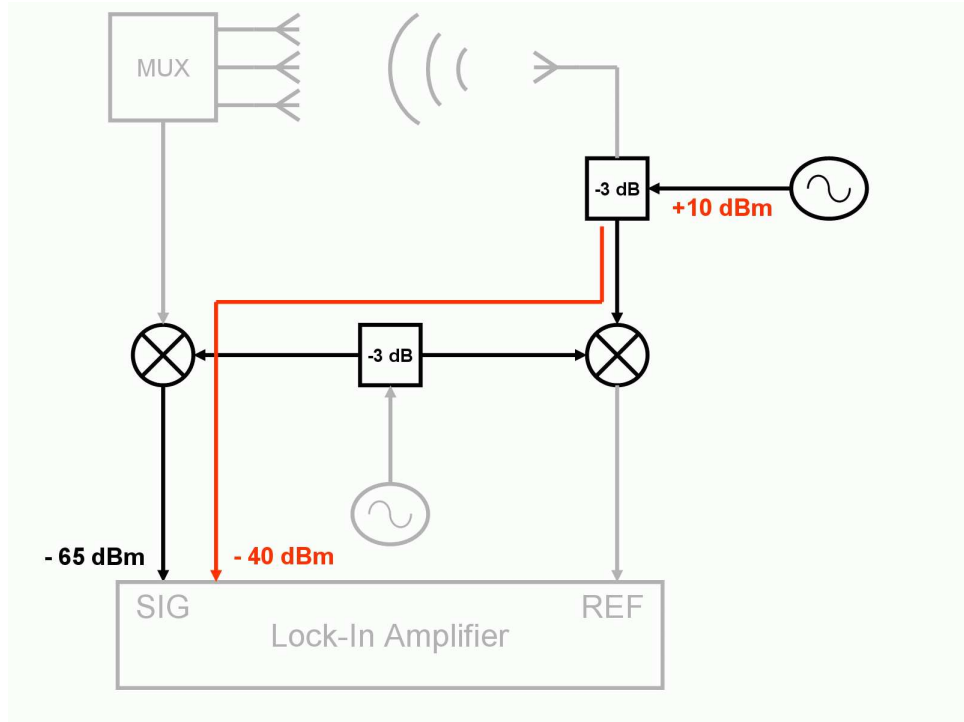


Figure 5.4: Signal path of the reference bleed-through to the SIG input.

5.6 Reference Signal Bleed-Through

An important flaw with the concept design becomes apparent when one considers the bleed-through experienced by the reference signal. Depicted in Figure 5.4, a path exists for the reference signal to find its way to the SIG input. Without sufficient isolation along this path, it is possible for the reference signal to overpower the SOI.

As the figure shows, the only impedance to the reference signal is the combined isolation of a mixer and a power divider. For a typical commercial mixer, the RF/LO isolation is on the order of -20 dB . Similarly, for a typical Wilkinson power divider, the isolation between output ports is also on the order of -20 dB . After a conversion loss of -7 dB at the second mixer, the reference signal has a bleed-through power of -40 dBm at the SIG input. In other words, the bleed-through from the reference channel overpowers the SOI by 25 dB .

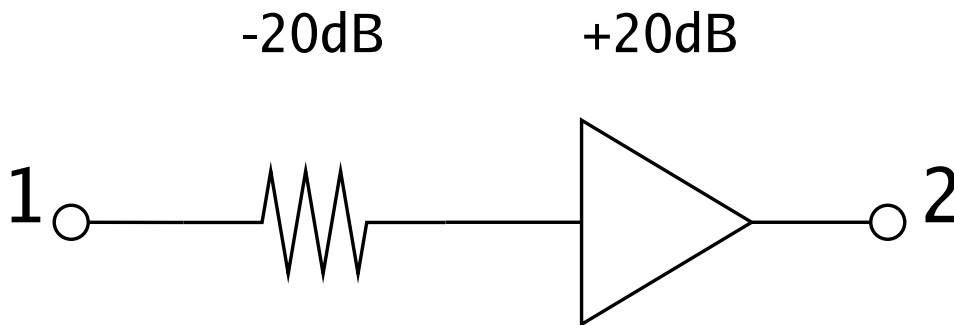


Figure 5.5: An isolator made from an amplifier-attenuator pair.

5.7 Bleed-Through Solution

The solution to this problem is an increase in SOI power and an increase in REF isolation. A simple way to increase the SOI power is to insert an amplifier after the AUT, therefore boosting the SOI by +20 dB or more. To increase the isolation from the REF signal, it is useful to employ the amplifier-attenuator pair shown in Figure 5.5. For a signal traveling in the forward direction (port 1 to port 2), the amplifier offsets the attenuator and nothing changes. For a signal traveling in the reverse direction, the directivity of the amplifier combines with the attenuator to drastically reduce the signal power. Thus, to a good approximation, the S-parameter matrix can be modeled as

$$S = \begin{bmatrix} 0 & \frac{1}{D+L} \\ \frac{G}{L} & 1 \end{bmatrix} \quad (5.4)$$

where D is the amplifier directivity, G is the amplifier gain, and L is the attenuator loss.

A good, high-isolation amplifier will have a directivity of at least $D = 30$ dB and should have a gain of at least of $G = 20$ dB. To offset the gain of the amplifier, the attenuator should then have a loss of $L = 20$ dB as well. The amplifier-attenuator pair therefore gives an extra 50 dB of isolation between mixer 1 and mixer 2. The final result is a power of -45 dBm from the SOI and a power of -93 dBm from the REF bleed-through. This implies a lower bound of $G_r = -45$ dBi before the

bleed-through from the reference signal is on the same order of magnitude as the SOI. In practice, however, it would be rare to expect any precision below -30 dBi.

5.8 Reference Input Power

Recall from Section 5.2 that the REF input to the LIA requires a signal strength of $400 \text{ mV}_{\text{pk-pk}}$ on a $1.0 \text{ M}\Omega$ impedance. For a characteristic impedance of 50Ω from the input line, this requires the REF input to have a minimum power level of -4 dBm. When compared to the calculated value of -3 dBm, the LIA is only marginally capable of locking in to the reference signal. To address this concern, an amplifier should be added at the REF input to the LIA with a gain of about $+10$ dB.

5.9 Low-Pass Filters

The final modification to the design requires two low-pass filters at the inputs. Because of harmonic distortion, upper-sideband mixing, and RF bleed-through, there exists the potential for high-frequency signals to make their way to the LIA inputs. To alleviate this concern, it is prudent to insert a low-pass filter with a cutoff frequency of 100 kHz at each input to the LIA.

5.10 Summary

The final receiver design is shown in Figure 5.6. Note that the design is basically the same as that in Figure 5.2, but with a few minor modifications to account for the non-ideal nature of the system. Particularly, the additions include an amplifier-attenuator pair to help isolate mixer 1 from mixer 2, two amplifiers to boost the SIG and REF powers, and two low-pass filters to remove the undesirable high-frequency content.

Currently, the receiver has no specified part numbers, since all of the testing was performed with devices that were literally scrounged out of boxes of spare parts. The current design has, however, been demonstrated on the prototype array feed, with excellent results. The final task, therefore, is to find commercial devices with

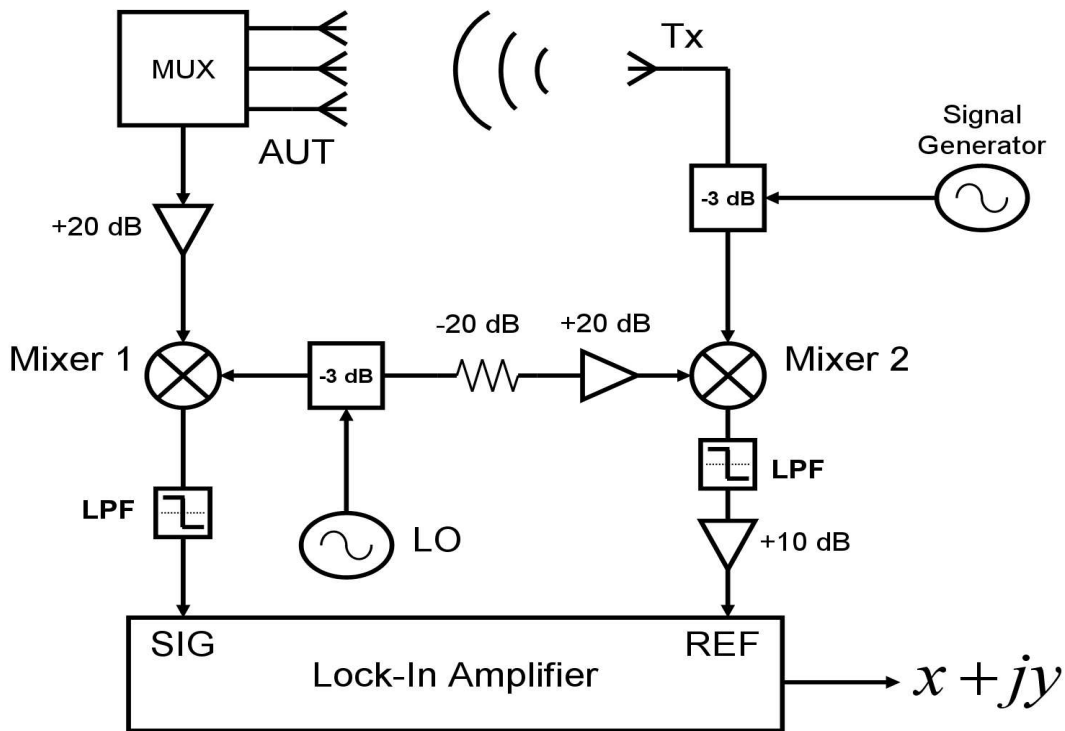


Figure 5.6: Final design for the NRAO test-range receiver.

which to construct a permanent receiver. Once this task has been completed, all future work with the range upgrade can be shifted to the user interface and data acquisition.

5.11 Array Directivity Measurements

In July, 2005, directivity measurements were performed on the array feed while using the prototype receiver design in Figure 5.6. An example of the experimental setup is depicted in Figure 5.7, which shows the array feed atop the rotating turret along the co-polarized, H-plane cut. For cut measurement, the phase center of rotation was fixed at the ground plane beneath the center element. For each phasor measurement, the load impedances at the other antenna elements were open-circuits.



Figure 5.7: The seven-element array at the NRAO test range in Green Bank, WV. The incident electric field is co-polarized with the array elements and the rotation is along the H-plane.

5.11.1 Calibration

From the geometry of the array, it is clear to see that the array elements are all coplanar when viewed from boresight. It is therefore reasonable to assume that an incident plane-wave from boresight should result in roughly identical excitations in every element. Using this assumption, it was possible to account for the relative variations in gain and phase delay between each channel. Note, however, that this information is only sufficient to produce a relative measurement of directivity. An absolute measurement was obtained in Section 4.4, which placed the boresight gain at 13 dBi.

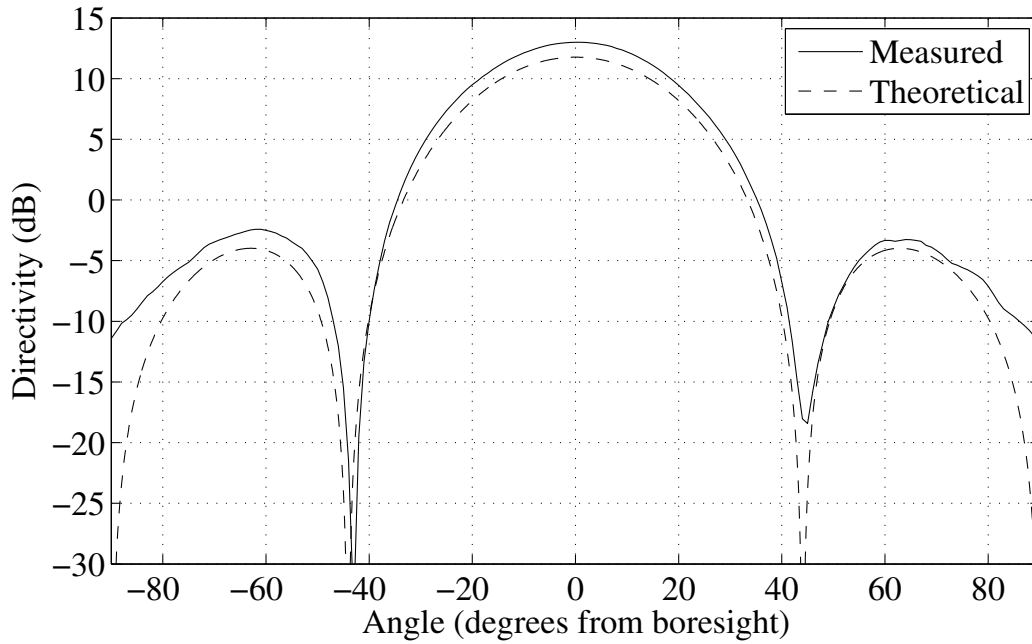


Figure 5.8: Co-polarized, H-plane cut pattern of the array feed compared with a theoretical Hertzian dipole model.

5.11.2 Directivity Results

Figure 5.8 shows the directivity measurement along the co-polarized H-plane cut with uniform array weighting. Also included is a theoretical comparison against the Hertzian dipole model from Section 2.1.2. Note that within 80° , the two plots agree very well. This is to be expected, since the element patterns are omnidirectional along this cut. Beyond 80° , the patterns begin to diverge, which is likely a result of the finite size of the physical ground plane. Similar results can be seen in Figure 5.9, which shows the co-polarized, E-plane cut with the same beamformer. Here, the agreement is good to within 45° , after which the element patterns are likely diverging from the Hertzian dipole model.

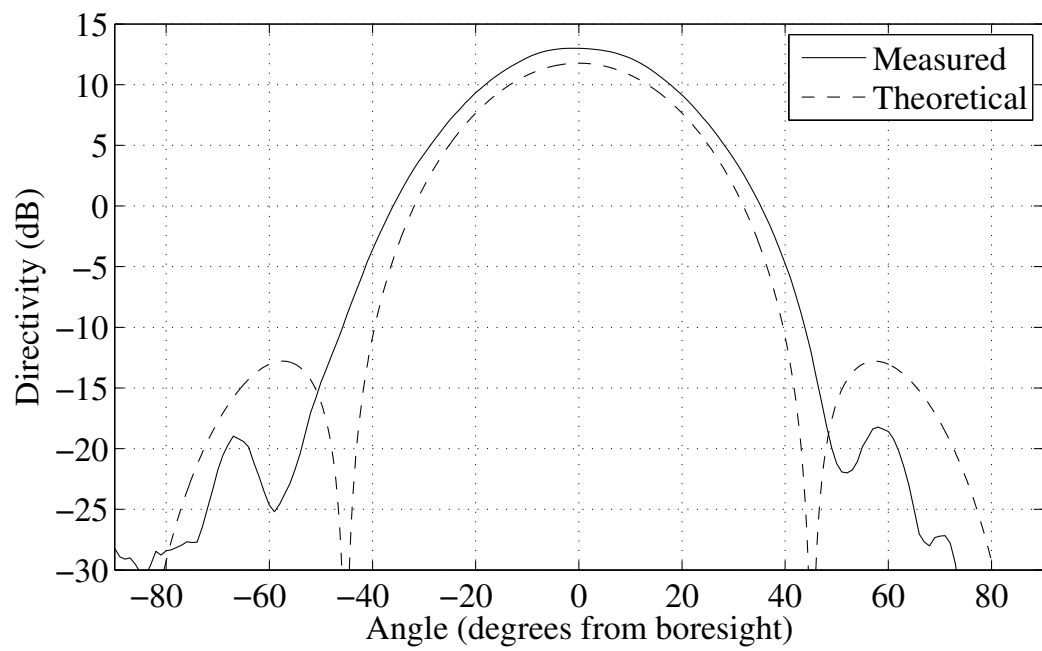


Figure 5.9: Co-polarized, E-plane cut pattern of the array feed compared with a theoretical Hertzian dipole model.

Chapter 6

RFI Mitigation with the Focal-Plane Array

This chapter describes the characterization of the focal plane array in conjunction with a three-meter parabolic reflector. It includes a description of the experimental setup, a boresight gain measurement, and the results of several RFI scenarios.

6.1 Experimental Setup

To simulate an astronomical observation in the presence of an interferer, the experiment required two transmitters and a receiver. One of the transmitters acted as a signal of interest (SOI) at boresight, while the other acted as an interferer in the deep sidelobes. To obtain a clear line of sight between the antennas, they were all positioned on separate rooftops among BYU campus. Figure 6.1 shows an overhead perspective of the antenna positions.

The receive antenna consisted of the prototype array feed mounted at the focal plane of a three-meter parabolic dish (Figure 6.2). Antenna 1 of the VSA was chosen for this role because it has a clear line of sight to the rooftops of BYU campus. The SOI was a standard gain horn positioned at boresight to the receiver. The roof of the Kimball Tower was a convenient place for this antenna, due to its easy access, large height, electrical outlets, and safety fencing. The interferer used a half-wave dipole antenna that rested on the observation deck of the Joseph F. Smith Building, which also has electrical access and safety fencing. In particular, when viewed from the Clyde Building, the observation deck spans a 4° arc from $27^\circ - 31^\circ$ relative to the SOI. This makes it ideal for testing array performance with a moving interferer.

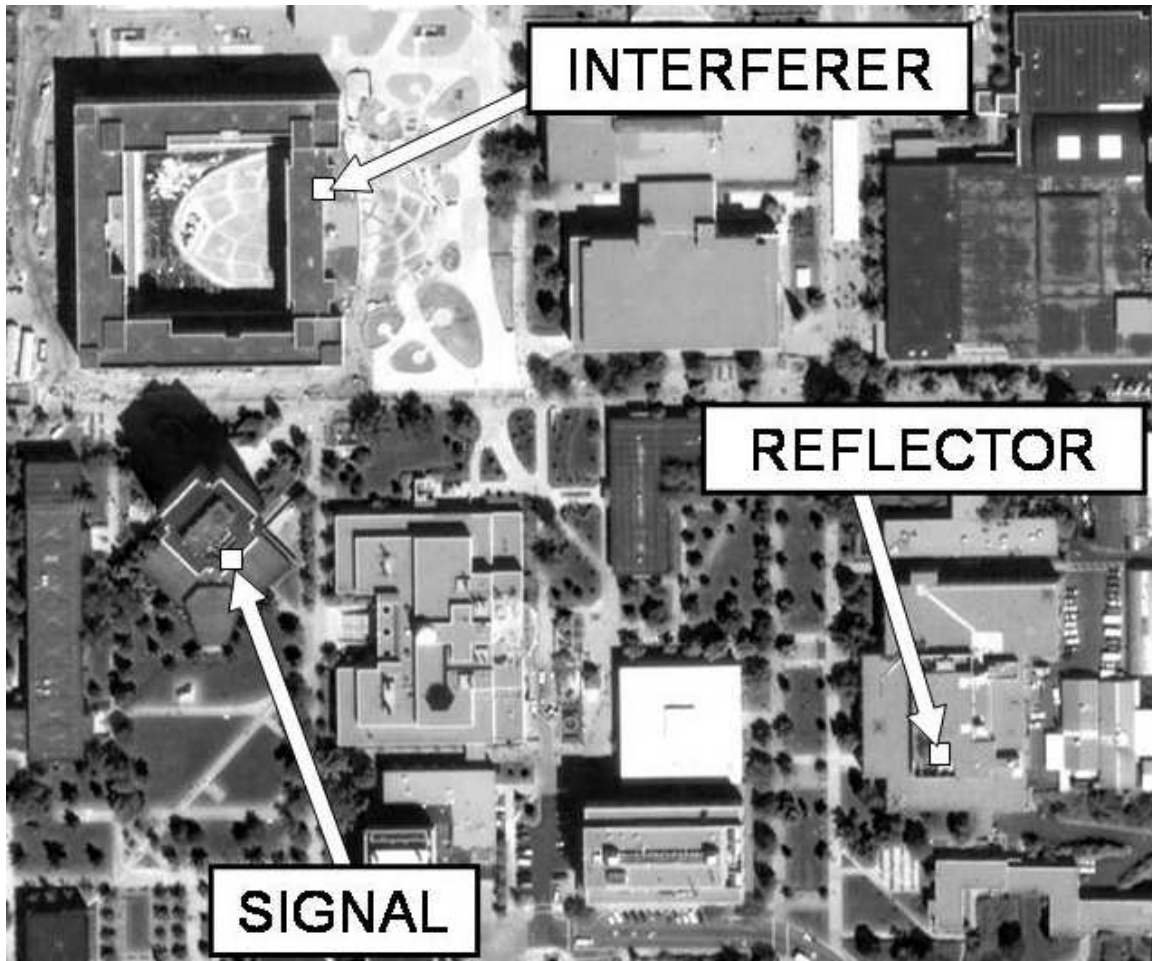


Figure 6.1: Rooftop positions of the antennas. The array feed and reflector are located on the roof of the Clyde Building. The horn antenna (signal) is positioned at boresight to the reflector and is located on the Kimball Tower. The interferer is a small dipole located on the observation deck of the Joseph F. Smith Building. Image taken from www.maps.google.com.



Figure 6.2: The array feed is mounted at the focal plane of a 3-meter reflector.

6.2 Calibration and Alignment

Before installing the array onto the reflector, the gain of each receiver channel was measured by feeding a continuous wave (CW), -110 dBm signal into each channel. The individual gains were then calculated by measuring the total power at the output and comparing with the known value at the input. This information provides meaningful units of voltage and power as seen by the individual antenna elements, which is necessary when calculating the effective area of the receiver or when using the array as a radiometer.

After calibration, the array was installed onto the support struts of Antenna 1. In order to accept the array feed, the support struts had to be modified by bending them outwards into a position that will fit with the array stand-offs. The center element of the array was located at the focal point of the dish, and the ground plane was parallel with the directrix plane of the reflector.

The final step was an alignment of the reflector so that it pointed directly at the SOI. This was accomplished by first activating the transmitter and broadcasting a strong, CW signal. The reflector was then scanned in azimuth and elevation until the power observed at the center element was maximized. The transmitter was similarly aligned by scanning the horn antenna in azimuth, elevation, and polarization until the observed power was maximized at the center element.

6.3 Training Data

Training data was obtained by sampling under controlled conditions. For example, the noise correlation matrix \mathbf{R}_{nn} was obtained by sampling while the SOI and the interferer were both deactivated. The signal correlation matrix \mathbf{R}_{ss} was obtained by sampling while the SOI was active with a very high SNR. Similarly, the interferer correlation matrix \mathbf{R}_{ii} was obtained by sampling while the interferer was active with a very high INR. The steering vectors \mathbf{d}_s and \mathbf{d}_i were obtained by computing the principle eigenvectors of their respective correlation matrices.

6.4 Effective Area and Aperture Efficiency

The effective area of the array feed was measured by using the same link-budget procedure as that in Section 4.4. After a simple modification of the Friis equation, the effective area of the center element in the array is given as

$$A_{eff} = \frac{4\pi r^2 P_{rec}}{G_t P_{rad}} \quad (6.1)$$

where r is the distance between the source and receive antennas, P_{rec} is the total received power at the center element, G_t is the gain of the transmit antenna, and P_{rad} is the total radiated power. The distance r was measured with a rangefinder and found to be 256 m. The transmit antenna was the same standard gain horn used in Section 4.4, which has a value of $G_t = 14$ dBi at 1600 MHz. The transmission from the signal generator was a CW waveform at -60 dBm, but the measured line losses and impedance mismatches subtracted 3 dB. Thus, the total radiated power was $P_{rad} = -63$ dBm.

The highest value for P_{rec} was obtained by using an adaptive LCMV beamformer given by

$$\mathbf{w} = \mathbf{R}_{xx}^{-1} \hat{\mathbf{d}}_s \quad (6.2)$$

The array weight vector \mathbf{w} was recalculated for every 4.9 ms segment of data¹ and the principle eigenvector of \mathbf{R}_{xx} was used for $\hat{\mathbf{d}}_s$. The total output power was then calculated using Equation 2.43,

$$P_{rec} = \frac{1}{\alpha_1 \alpha_2} \mathbf{w}^H \mathbf{R}_{ss} \mathbf{w}$$

where α_1 and α_2 were calculated using the methods outlined in Section 4.4. The result was a total received power of -101.6 dBm, which yields an effective area of 4.56 m². For a physical reflector area A_{phy} , the *aperture efficiency* η_{ap} is defined as

$$\eta_{ap} = \frac{A_{eff}}{A_{phy}} \quad (6.3)$$

For a diameter of 3.0 meters at rim of the reflector, the physical collecting area is 7.07 m², and the aperture efficiency is found to be 0.64. This compares well with the

¹ 4.9 ms represents a single block of unpacked data, and therefore made a convenient choice from a programming perspective.

aperture efficiencies of standard reflector antennas. For example, a reflector antenna that is optimized for gain can reach an aperture efficiency as high as 0.80. Often times, however, gain will be traded off for lower spillover efficiency, and typically results in an aperture efficiency as low as 0.55.

It is important to note that because of antenna misalignments, multipath, loss uncertainties, and gain variations, the confidence for these measurements is on the order of ± 1.0 dB in the signal path. The only way to reliably reduce this uncertainty would be to repeat the entire measurement inside an anechoic chamber, which is impractical. Converting this uncertainty into the effective area gives a lower bound at 3.62 m^2 ($\rho = 0.51$), and an upper bound of 5.74 m^2 ($\rho = 0.81$).

6.5 Stationary Interferer

The first interference scenario was a weak SOI in the presence of a powerful interferer. The SOI was a CW transmission at 1611.3 MHz with an output power of -110 dBm. This value was chosen because it placed the SOI below the non-integrated noise floor of the receiver. The interferer was a 0 dBm FM transmission centered at 1611.3 MHz, with 30 kHz of deviation and 1.0 kHz of modulation. This scenario represents a typical encounter in radio astronomy where a weak SOI is overpowered by an off-boresight interferer at the same frequency.

6.5.1 Single Element

Figure 6.3 shows the non-integrated power spectral density (PSD) of the signal as seen by the center element of the array. To reduce spectral leakage, the data has been windowed by a Hanning function. Also, to flatten out the noise floor, a baseline subtraction was performed by dividing out the PSD of a noise-only data set. This graph represents the control signal that would be seen by a standard, single-feed receiver in a radio telescope. Because the SOI is so weak, the only way to distinguish it from the noise floor is through integration.

Figure 6.4 shows the resulting PSD after 10 seconds of integration. As expected, the noise floor is smoothed out, but the FM interferer remains and the SOI is

not resolved. If this were an actual scientific observation, the data would be useless and the observation would have to be discarded.

6.5.2 Max SINR using Interferer Subspace Partitioning

Because the interferer was so much more powerful than the noise floor or the SOI, it was possible to solve for the max-SINR beamformer through a process called *interferer subspace partitioning* (ISP). ISP works by using the principle eigenvector of \mathbf{R}_{xx} as an estimate for $\hat{\mathbf{d}}_i^2$. The interferer correlation matrix \mathbf{R}_{ii} is then estimated by using

$$\hat{\mathbf{R}}_{ii} = \hat{\mathbf{d}}_i \hat{\mathbf{d}}_i^H . \quad (6.4)$$

The interference-plus-noise correlation matrix $\hat{\mathbf{R}}_{NN}$ is estimated by using $\hat{\mathbf{R}}_{NN} = \hat{\mathbf{R}}_{ii} + \mathbf{R}_{nn}$, where \mathbf{R}_{nn} is obtained from training data. Finally, the array weight vector \mathbf{w} is given by the principle eigenvector to the generalized eigenvalue problem,

$$\mathbf{R}_{ss} \mathbf{w} = (\text{SINR}) \hat{\mathbf{R}}_{NN} \mathbf{w} \quad (6.5)$$

which is simply the max-SINR beamformer. Figure 6.5 shows the results from this method using an update rate of 4.9 ms. As can be seen, the FM interferer is almost completely removed and the SOI is recovered.

6.6 Non-stationary Interferer

A more typical encounter in radio astronomy is a non-stationary interferer, such as radar bounce from an aircraft, satellite broadcasts, or the relative motion of the telescope while tracking an object in the sky. This situation was simulated by carrying the interfering antenna along the observation deck of the Joseph F. Smith Building and walking at a normal pace. As seen from the receiver at the Clyde Building, the angular velocity was on the order of $0.1^\circ/s$, which is typical for a satellite in medium Earth orbit. During this trial, the SOI was a CW transmission at -90 dBm with a -10 dBm FM interferer overlapping in frequency.

² See section 2.2.1

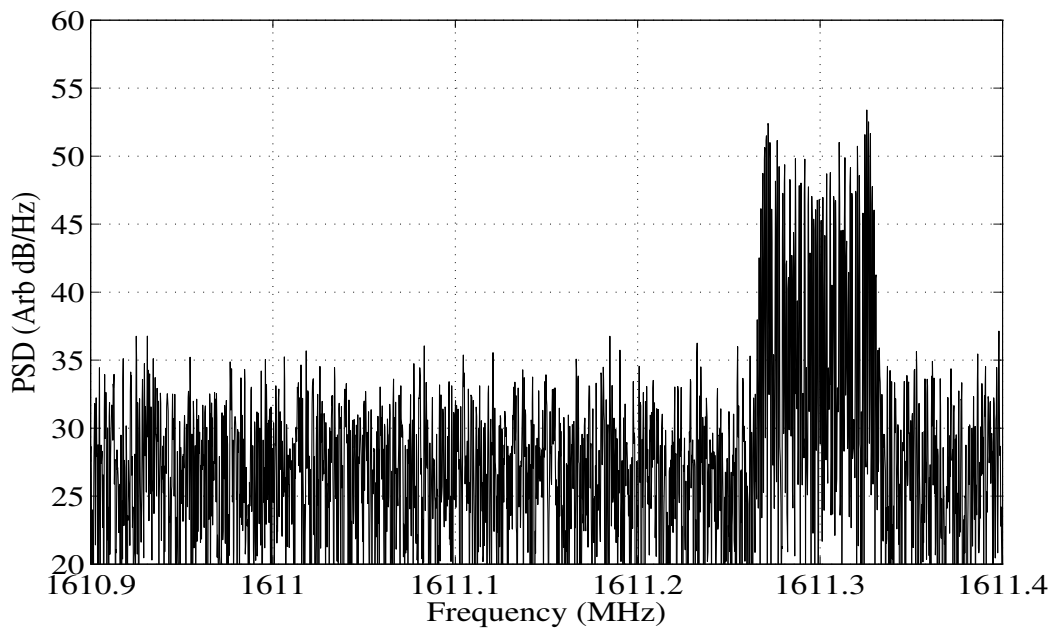


Figure 6.3: Non-integrated PSD as seen by the center element alone. A CW signal is buried beneath the noise floor with an FM interferer overlapping. Due to baseline subtraction, the units for power are arbitrary.

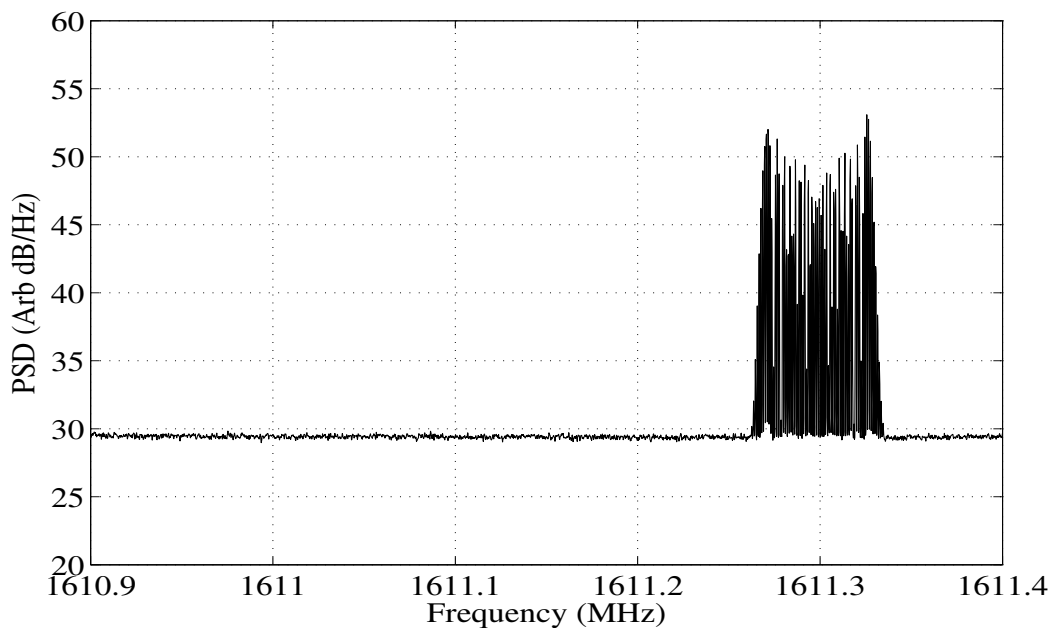


Figure 6.4: PSD of the center element after 10 seconds of integration. The noise floor is smoothed out, but the FM interferer remains and completely masks the signal of interest.

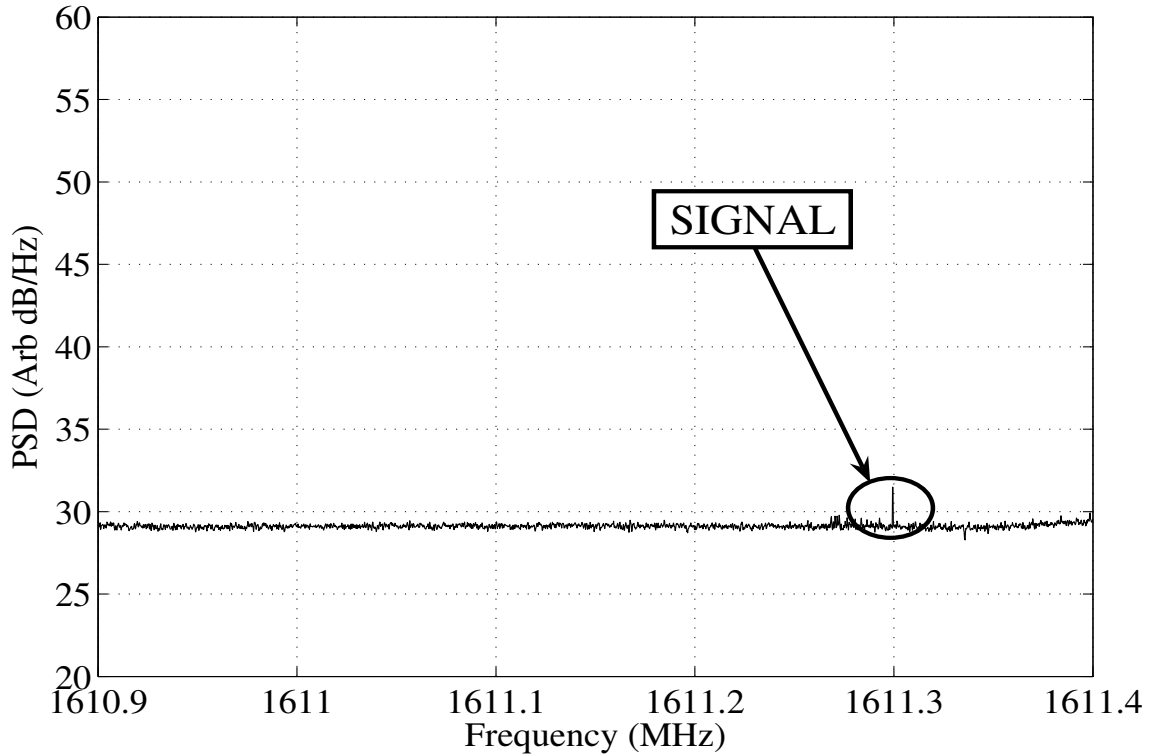


Figure 6.5: PSD of the Max-SINR beamformer using interferer subspace partitioning on the stationary interferer. The total integration time is 10 seconds. Note how the interferer is almost completely removed and the signal is recovered.

6.6.1 Single Element

Figure 6.6 shows the PSD as seen by the center element with 10 seconds of integration on the non-stationary interferer. As expected, the interferer dominates the signal and the SOI is not apparent.

6.6.2 Max SINR using Interferer Subspace Partitioning

Figure 6.7 shows the max-SINR beamformer from Section 6.5.2 with an update every 4.9 ms. Even though it was non-stationary, the interferer has been mitigated and the SOI is recovered.

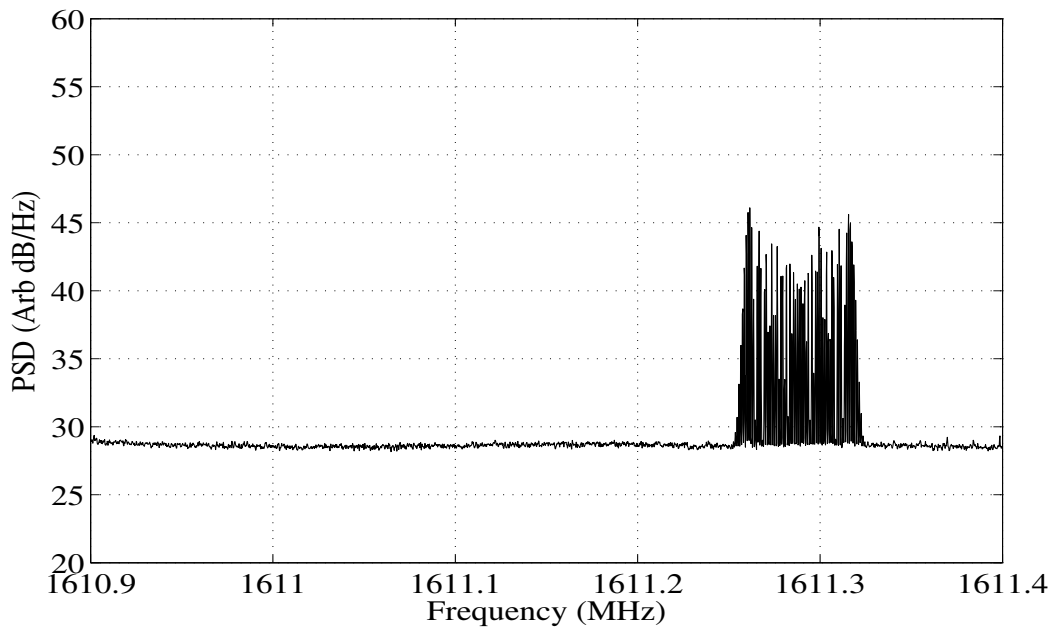


Figure 6.6: PSD as seen by the center element after 10 seconds of integration. The interferer is traveling at a velocity of approximately $0.1^\circ/\text{s}$.

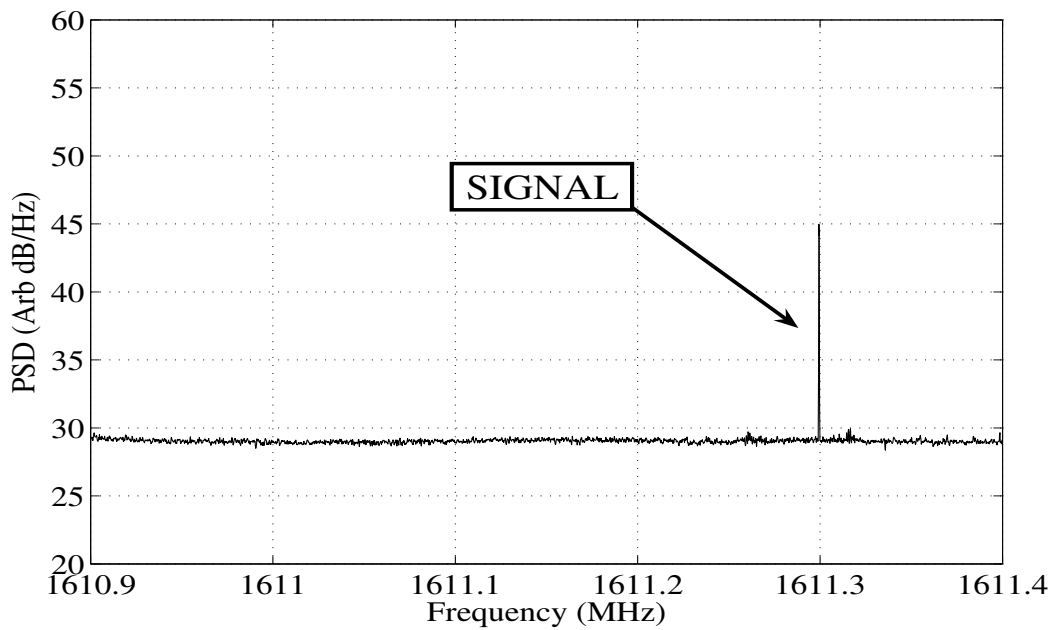


Figure 6.7: PSD of the Max-SINR beamformer using interferer subspace partitioning on the moving interferer. The total integration time is 10 seconds. Again, the interferer is almost completely removed and the signal is recovered.

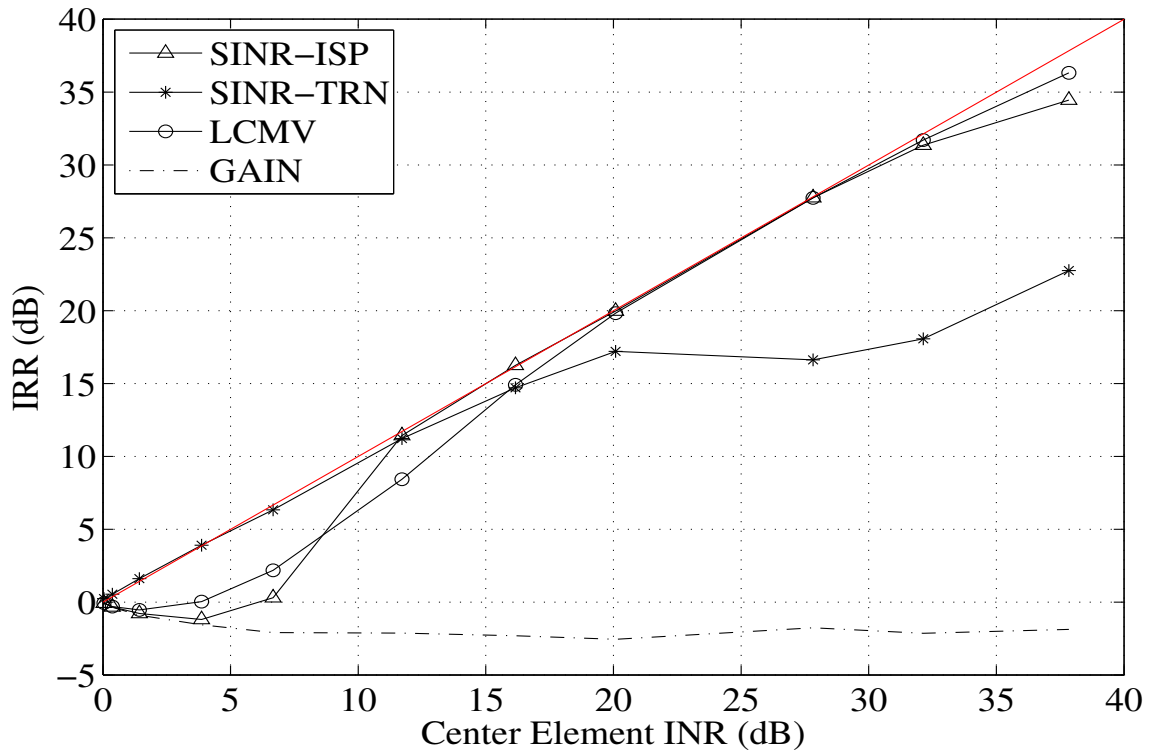


Figure 6.8: Interference rejection ratio of the beamformers as a function of interference to noise ratio at the center element. The red line represents $y = x$, which indicates the interferer is either at or below the noise floor.

6.7 Performance Versus Interferer Power

The performance of a given beamformer depends greatly on the relative power levels between the signal and the interferer. To measure this effect, several measurements were taken with a varying amount of input power from the interferer. A useful metric for beamformer performance is the interference rejection ratio (IRR), which is defined as the INR seen by the center element (INR_{el1}) divided by the INR as seen by the beamformer of interest (INR_x), and written as

$$\text{IRR} = \frac{\text{INR}_{el1}}{\text{INR}_x}. \quad (6.6)$$

Figure 6.8 summarizes the performance of several beamformer techniques as a function of interferer power level. The first beamformer (SINR-ISP) represents

max-SINR using interferer subspace partitioning with an update every 4.9 ms. The second beamformer (SINR-TRN) represents a single max-SINR beamformer calculated once from training data. The third beamformer (LCMV) represents the LCMV beamformer with an update every 4.9 ms. The fourth beamformer (GAIN) is a single max-gain beamformer calculated from training data, and represents a control signal without any interference mitigation at all.

It is interesting to note how there is no ideal beamformer for the entire range of interferer power. At low power levels (< 10 dB), the best results were obtained by using the SINR-TRN beamformer, which seems to provide a relatively fixed amount of interference rejection on the order of 18 dB. At medium power levels (10 - 25 dB), the best results were obtained from the SINR-ISP beamformer, with LCMV following closely. At high power levels (> 25 dB), LCMV and SINR-ISP begin to wane, but with LCMV performing better. As expected, the max-gain beamformer provided no interference rejection, but rather increased the power in the interferer, as indicated by the negative IRR.

6.8 Correlation Time and Non-Stationarity

When calculating a correlation matrix, it is generally preferable to average for as long as possible in order to reduce estimation error caused by noise. A moving interferer, however, has non-stationary statistics. This places an upper limit to the length of a correlation window before non-stationarity influences an estimate. Thus, there is an inherent trade-off in the estimation error. If the correlation window is too short, then estimation error is dominated by noise. If the correlation window is too long, then estimation error is dominated by non-stationarity.

Figure 6.9 shows the IRR of two beamformers as a function of correlation time, where the data set is the stationary interferer. As expected, the IRR is low over short correlation windows because the correlation estimate is dominated by noise. However, there is also an upper limit to the benefits of averaging a correlation matrix. After 5 ms or so, the IRR levels off and shows no improvement over longer averaging windows.

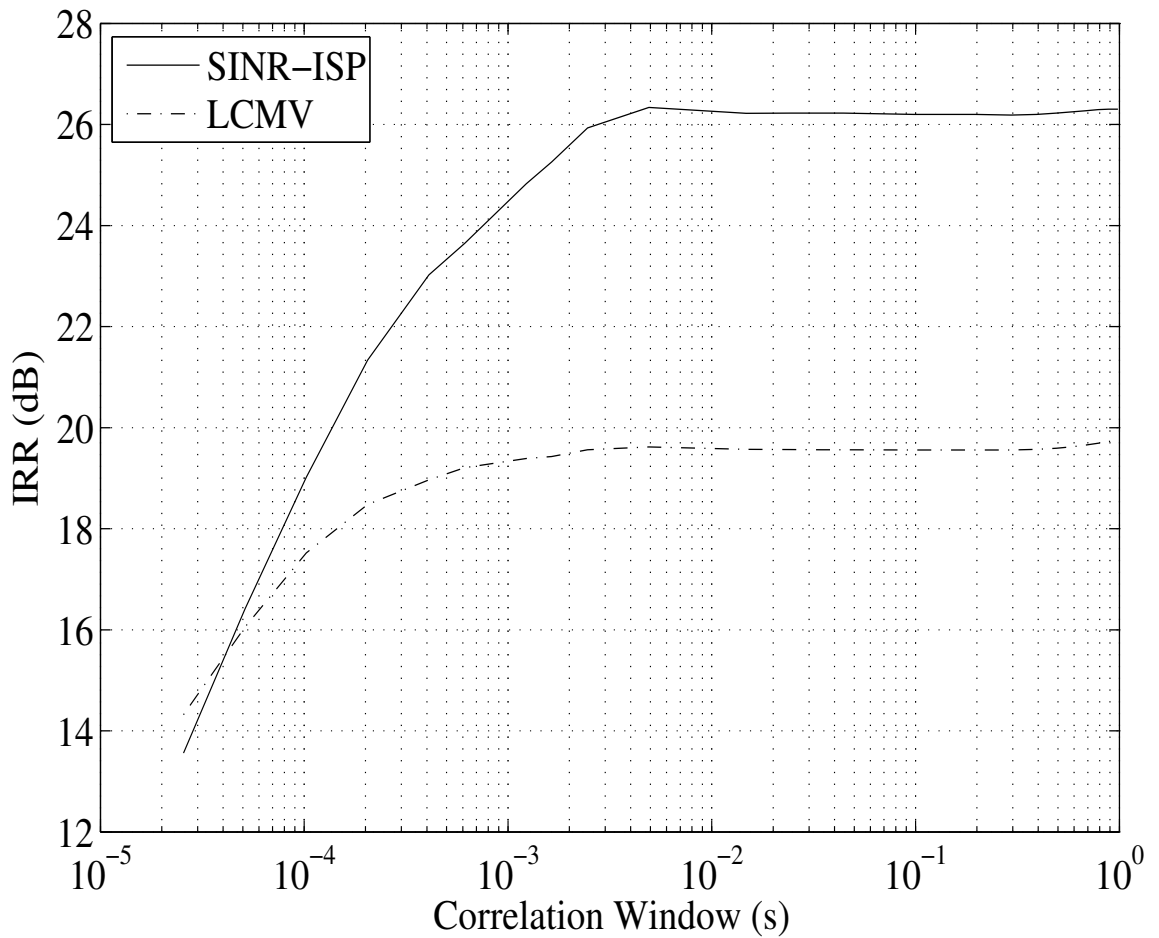


Figure 6.9: Interference rejection ratio as a function of correlation length for the stationary interferer.

It is interesting to note how subspace partitioning results in much greater interference mitigation than LCMV. It is also interesting to note how long-term correlation does not perfectly mitigate the interferer. This is likely the result of small-scale non-stationarity in the interferer correlation matrix. Minor perturbations due to mechanical vibration and multipath can cause the instantaneous correlation matrix to deviate slightly from its mean value. The interference rejection is therefore very high, but can not perfectly track the instantaneous changes.

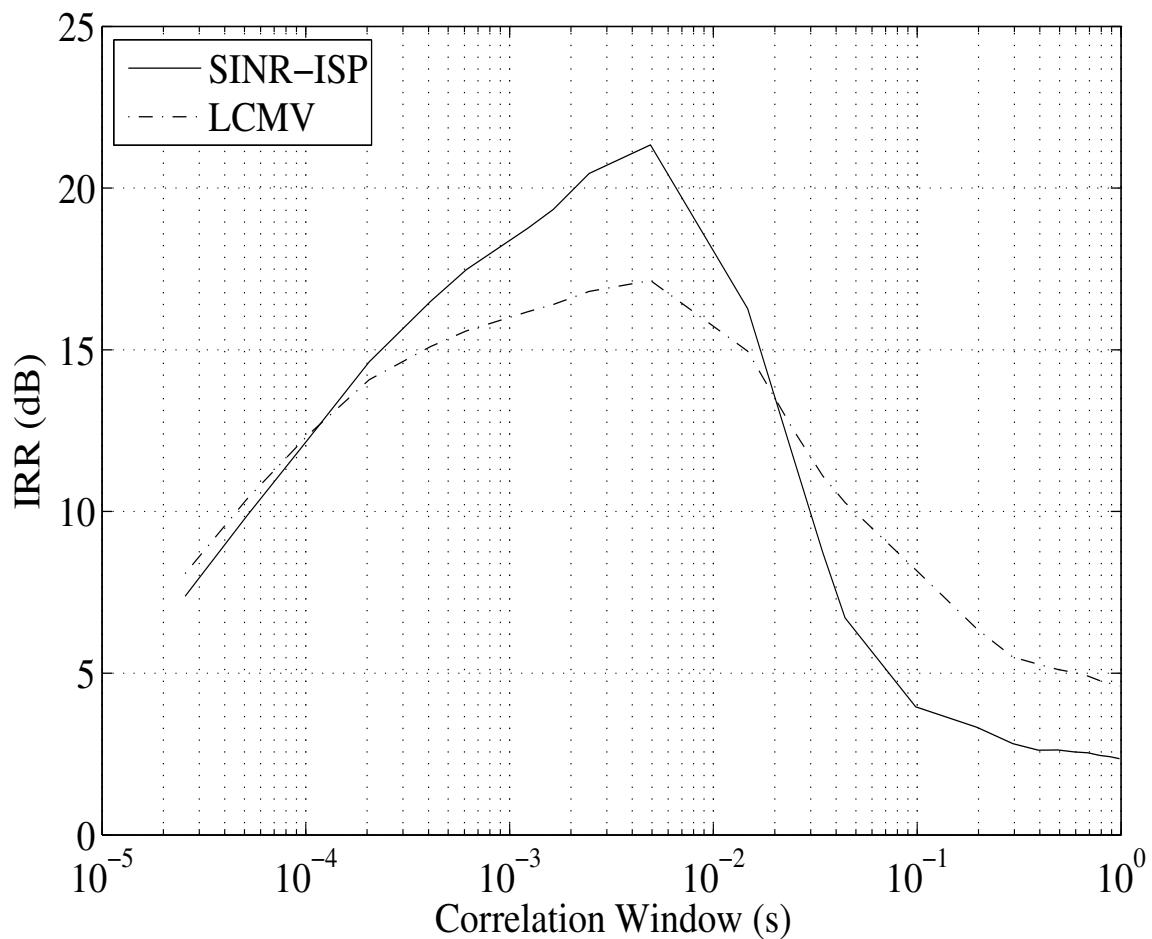


Figure 6.10: Interference rejection ratio as a function of correlation length for the moving interferer.

Figure 6.10 shows IRR as a function of correlation time for the moving interferer. As can be seen, the IRR begins to drop significantly after 5 ms. This is to be expected, since the interferer was physically moving. In other words, any estimate of the interferer correlation is only valid for a short time, since the interferer physically moves out of the spatial null. Consequently, the beamformers lose performance after long correlations. These results demonstrate the need for rapid updates in a beamformer. Otherwise, the non-stationary statistics can potentially invalidate any estimate of a correlation.

6.9 Pattern Rumble

As an interferer moves in direction, the updates in an adaptive beamformer will modify the beam pattern as it tracks the spatial null. As this null moves in position, it will perturb the rest of the beam pattern as well, causing variation in antenna response to the spillover noise and SOI. This phenomenon, called *pattern rumble*, is undesirable because it reduces the sensitivity of the receiver.

Even if the interferer is not physically moving, pattern rumble can still emerge from other sources. Interferer multipath can introduce significant statistical variation if the channel is not stationary. Mechanical vibrations in the reflector are also a concern because they perturb the direction of arrival for the interferer. Another potential source of pattern rumble is *weight jitter*, which is an effect caused by the inversion of the correlation matrix \mathbf{R}_{xx} . Because this matrix includes noise information, the high-order eigenvalues introduce a significant variability into the array weight updates [26].

The sensitivity of a radio telescope is often measured by the *minimum detectable signal* ΔT_{min} , which is given by the formula

$$\Delta T_{min} = \frac{T_{sys}}{\sqrt{Bt}} \quad (6.7)$$

where T_{sys} represents the system noise temperature, B represents the noise bandwidth, and t represents the integration time. The significance of Equation 6.7 is that an arbitrarily weak signal should be detectable after a sufficient length of integration time. In practice, however, the instability in a radio receiver places an upper limit on the benefits of integration. This is modeled by rewriting Equation 6.7 as [27]

$$\Delta T_{min} = T_{sys} \sqrt{\frac{1}{Bt} + \left(\frac{\Delta G}{\bar{G}}\right)^2} \quad (6.8)$$

where \bar{G} is the average gain of the receiver and ΔG is the standard deviation of the receiver gain. Thus, the benefits of long-term integration are limited by the quantity $\Delta G/\bar{G}$.

For a single-feed antenna, a high-quality receiver can easily reduce $\Delta G/\bar{G}$ to a very small value. When updating an adaptive beamformer, however, $\Delta G/\bar{G}$ can

increase by a great deal. The reason is because pattern rumble effectively changes the beamformer response to the SOI and noise. As seen by the receiver, the result is equivalent to an increase in ΔG .

To understand how pattern rumble affects the final sensitivity, consider the turning point where pattern rumble overpowers the noise variance. This is the point at which

$$\frac{1}{Bt} = \left(\frac{\Delta G}{\bar{G}} \right)^2 . \quad (6.9)$$

For perspective purposes, a standard bandwidth is chosen as $B_0 = 1.0$ kHz. The maximum integration time t_{max} is then defined as

$$t_{max} = \frac{1}{B_0 \left(\frac{\Delta G}{\bar{G}} \right)^2} . \quad (6.10)$$

In other words, t_{max} represents the maximum integration time where the noise variance, at a bandwidth of B_0 , is stronger than receiver instability. Integration beyond this time will still decrease ΔT_{min} , but the marginal benefit approaches zero.

If the amplifier gain of each channel is assumed to be relatively constant, then the quantity $\Delta G/\bar{G}$ is dominated by pattern rumble. It can therefore be measured as the time-variation in SNR from the adaptive beamformer. Note, however, that pattern rumble is not the only phenomenon that can introduce jitter in the SNR. For example, mechanical vibrations in the reflector will introduce jitter in the SOI that is independent of the pattern rumble. It should also be noted that the measured noise floor periodically rose and fell by roughly 1.0 dB. This was likely the result of broadband interference that reflected off of the Kimball Tower and into the main beam of the receiver.³

To normalize these effects, the array gain G_a was measured against the max-gain beamformer (which uses non-updating weights) such that

$$G = G_a = \frac{\text{SNR}_x}{\text{SNR}_{gain}} . \quad (6.11)$$

³ Similar interference has been observed at the same frequencies reflecting off other buildings in the area.

This expression effectively cancels out the effects of outside influences, since the variations in SNR will be roughly the same for both beamformers. Thus, the remaining jitter should be due to pattern rumble from the adaptive beamformer.

Figure 6.11 shows the observed pattern rumble for three adaptive beamformers acting on the fixed interferer. Each point represents a sliding window of one-second integration before calculating G_a . The SINR-TRN beamformer represents a control signal because it used fixed weights, while LCMV and SINR-ISP were updated every 4.9 ms. From the data, the maximum integration times were calculated as 1.7 seconds for SINR-TRN, 1.7 seconds for LCMV, and 1.2 seconds for SINR-ISP. Thus, the observed pattern rumble for the updated beamformers was on the same order of magnitude as the fixed-weight beamformer. This result suggests that mitigation of a stationary beamformer does not introduce any significant pattern rumble above the natural rumble of the system.

Figure 6.12 shows the observed pattern rumbles for the case of the moving interferer. In this case, the maximum integration time for the SINR-TRN beamformer was slightly higher, measuring at a value of 3.3 seconds. The updated beamformers, however, measured significantly lower, both reaching a maximum integration time of only 0.3 seconds. This result shows how adaptively mitigating an interferer can reduce the effective sensitivity of a radio telescope by as much as one-tenth. In the future, it may be possible to construct a beamformer that minimizes this effect, but further research will be required.

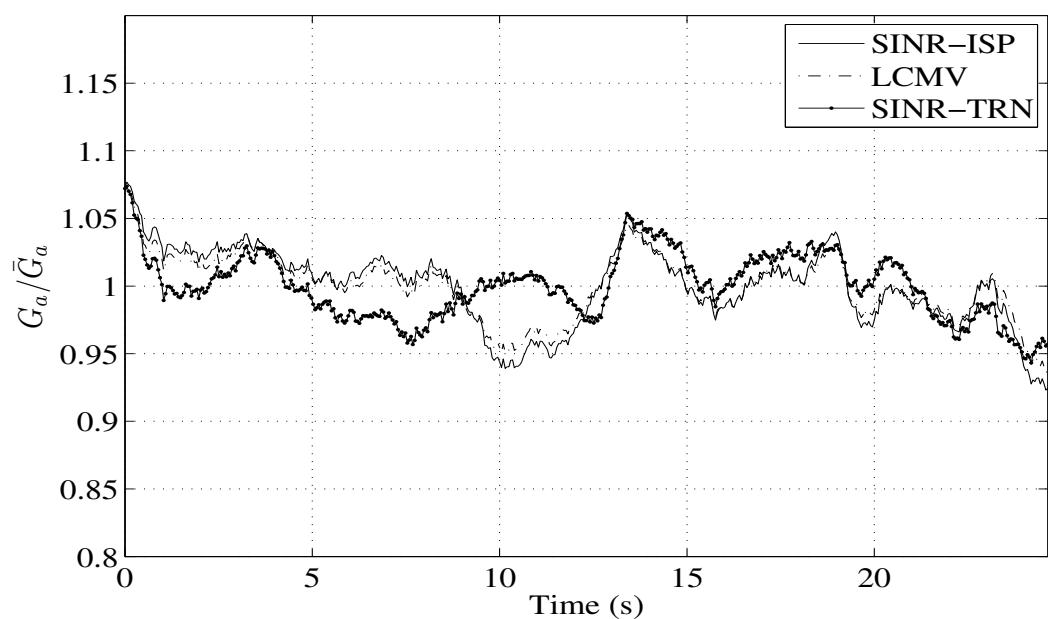


Figure 6.11: Pattern rumble for the stationary interferer. The maximum integration time is roughly 1.7 seconds.

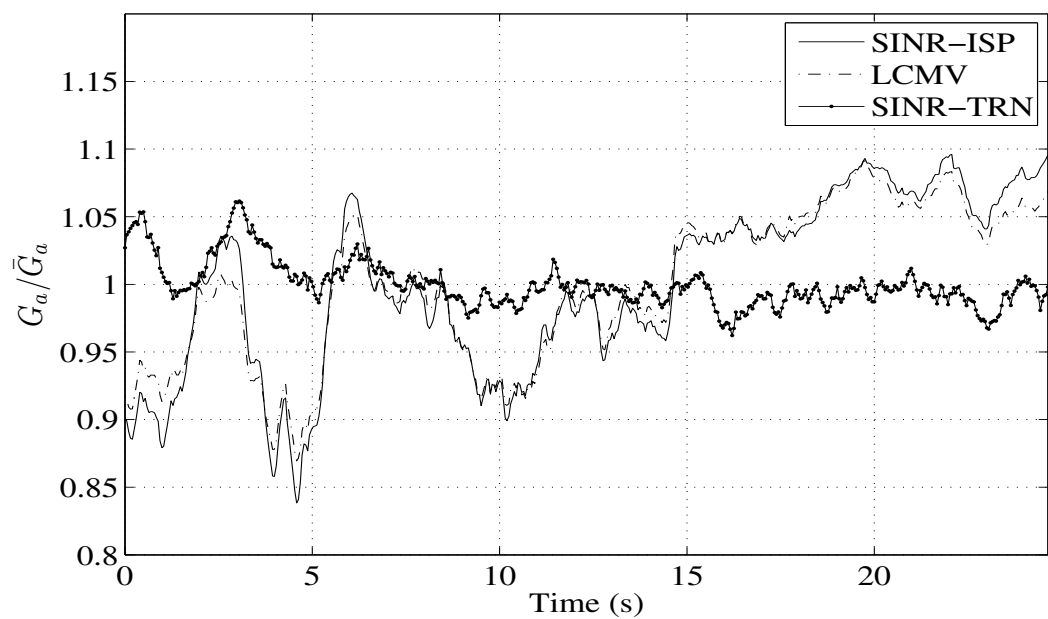


Figure 6.12: Pattern rumble for the moving interferer. The maximum integration time is roughly 3.3 seconds for the fixed-weight beamformer and 0.3 seconds for the updated beamformers.

Chapter 7

Conclusions and Future Work

The primary contribution of this thesis has been the design and construction of a seven-element array feed with seven corresponding receiver channels. The array was then demonstrated by mitigating a strong interferer to recover a weak signal of interest. The results of that demonstration have proven useful in characterizing the array feed, as well as in highlighting the major problems that need to be solved. The following sections discuss several of the outstanding issues that will require future research.

7.1 Robust Beamformers

Paradoxically, the stronger an interferer is, the more effectively it can be mitigated. When the interfering signal is on the same order of power as the signal of interest, however, it becomes far more difficult to mitigate. Little research has been applied towards this issue, since it is not as important to communications or radar applications as it is to radio astronomy. Many solutions have been suggested, such as subspace-tracking and multiple null placement [26], but they have yet to be demonstrated with an array feed.

7.2 Array Weight Normalization

In order to be useful as a radiometer, it is important to properly scale the output of a beamformer. Otherwise, the array weights will artificially add power to the final signal. Mathematically, this is accomplished by enforcing the criterion

$$\mathbf{w}^H \mathbf{A} \mathbf{w} = 1 \tag{7.1}$$

where \mathbf{A} is the pattern overlap matrix. The problem with this condition is that \mathbf{A} is rarely available, which means the final power as seen by the array is difficult to precisely measure. Although the identity matrix makes for a reasonable approximation, the requirements of radio astronomy are too precise for it to be used with astronomical signals.

7.3 Optimal Feed Placement

The placement of the array can have a significant impact on the performance of the receiver. For the experiments in Chapter 6, the array feed was placed such that the center element was at the focal point of the reflector. This placement was *ad hoc*, however, because there was little research available that might suggest a more ideal location. It is possible that the array would perform better if the focal point were located at the ground plane below the center element, but the only way to be sure would be to measure (or simulate) the array gain at varying locations.

7.4 Mutual Coupling

Mutual coupling has the potential to lower sensitivity, increase noise temperature, and impair the performance of a beamformer. It is possible to alleviate this problem through the use of matching networks, but this has yet to be extensively studied or implemented with the array feed.

7.5 Sensitivity

Although the aperture efficiency of the array feed performed well, the most important metric to radio astronomers is sensitivity. Measuring this will require a measurement of spillover efficiency, as well as a deeper understanding about mutual coupling and pattern rumble.

7.6 Array Expansion

Currently, there is work in progress to expand the number of array elements from 7 to 19. With more array elements, it would be possible to mitigate more

independent interferers with less trade-off in sensitivity. Due to its physical size and weight, however, it is unlikely that a 19-element array would be compatible with our 3 meter dishes. A larger reflector would experience less signal blockage and also be capable of mechanically supporting the extra weight.

7.7 Astronomical Observation on the GBT

The ultimate goal for the array feed is to demonstrate its performance on the Green Bank Telescope (GBT), and any design choices should be made with this goal in mind. If a focal plane array were used to mitigate a real satellite interferer and recover a legitimate astronomical signal, then it will have proven its usefulness to the radio astronomy community.

Bibliography

- [1] H. Rottgering, “LOFAR, a new low frequency radio telescope,” *New Astronomy Reviews*, vol. 47, no. 2, pp. 405–409, September 2003. 2
- [2] D. DeBoer, W. J. Welch, J. Dreher, J. Tarter, L. Blitz, M. Davis, M. Fleming, D. Bock, G. Bower, J. Lugten, Girmay-Keleta, L. D’Addario, G. Harp, R. Ackermann, S. Weinreb, G. Engargiola, D. Thornton, and N. Wadefalk, “The Allen telescope array,” *Proceedings of the SPIE*, vol. 5489, pp. 1021–1028, 2004. 2
- [3] P. J. Hall, *The Square Kilometre Array: An Engineering Perspective*, 1st ed. Springer, 2005. 2
- [4] J. R. Fisher, “Signal analysis and blanking experiments on DME interference,” NRAO Electronics Division, Tech. Rep. 313, April 2004. 2
- [5] S. Ellingson, J. Bunton, and J. Bell, “Removal of the GLONASS C/A signal from OH spectral line observations using a parametric modeling technique,” *The Astrophysical Journal Supplement Series*, no. 135, pp. 87–93, July 2001. 2
- [6] B. Smolders and G. Hampson, “Deterministic RF nulling in phased arrays for the next generation of radio telescopes,” *IEEE Transactions on Antennas and Propagation*, vol. 44, no. 8, pp. 13–22, 2002. 2
- [7] J. L. Campbell, “The development of a small scale radio astronomy image synthesis array for research in radio frequency interference mitigation,” Master’s thesis, Brigham Young University, 2005. 2
- [8] A. J. Poulsen, “Real-time adaptive cancellation of satellite interference in radio astronomy,” Master’s thesis, Brigham Young University, 2003. 2

- [9] B. D. Jeffs, L. Li, and K. F. Warnick, “Auxiliary antenna-assisted interference mitigation for radio astronomy arrays,” *IEEE Transactions on Signal Processing*, vol. 53, no. 2, pp. 439–451, February 2005. 2
- [10] C. K. Hansen, “Beamforming techniques and interference mitigation using a multiple feed array for radio astronomy,” Master’s thesis, Brigham Young University, 2004. 2
- [11] S. J. Blank and W. A. Imbraile, “Array feed synthesis for correction of reflector distortion and verneir beamsteering,” *IEEE Transactions on Antennas and Propagation*, vol. 36, no. 10, pp. 1351–1358, October 1988. 2
- [12] L. Staveley-Smith, W. E. Wilson, T. S. Bird, M. J. Disney, R. D. kers, K. C. Freeman, R. F. Haynes, M. W. Sinclair, R. A. Vaile, R. L. Webster, and A. E. Wright, “The Parkes 21-cm multibeam receiver,” *Publications of the Astronomical Society of Australia*, vol. 13, pp. 243–248, 1996. 2
- [13] B. S. Koribalski, “The H1 Parkes all-sky survey (HIPASS),” *ASP Convergence Series*, vol. 276, p. 72, October 2002. 2
- [14] M. V. Ivashina, J. G. bij de Vaate, R. Braun, and J. Bregman, “Focal plane arrays for large reflector antennas: First results of a demonstrator project,” *Proceedings of the SPIE*, vol. 5489, pp. 1127–1138, September 2004. 2
- [15] J. R. Fisher and R. F. Bradley, “Full-sampling array feeds for radio telescopes,” *Proceedings of the SPIE*, vol. 4015, pp. 308–319, 2000. 2
- [16] C. K. Hansen, K. F. Warnick, B. D. Jeffs, J. R. Fisher, and R. Bradley, “Interference mitigation using a focal plane array,” *Radio Science*, vol. 40, June 2005. 3, 13, 31
- [17] B. T. Walkenhorst, “Development of a radio telescope receiver for research in radio astronomy interference mitigation,” Master’s thesis, Brigham Young University, 2001. 3, 15

- [18] J. Li and P. Stoica, *Robust Adaptive Beamforming*. John Wiley & Sons, Inc, 2006. 5
- [19] J. A. Kong, *Electromagnetic Wave Theory*. EMW Publishing, 2000. 7
- [20] T. K. Moon and W. C. Stirling, *Mathematical Methods and Algorithms for Signal Processing*. Prentice Hall, 2000. 13
- [21] K. F. Warnick and B. D. Jeffs, “Receive array gain and aperture efficiency,” 2006. 14
- [22] D. M. Pozar, *Microwave Engineering*, 2nd ed. Wiley, 1998. 26
- [23] J. R. Fisher and R. F. Bradley, “Full-sampling focal plane array,” *Imaging at Radio Through Submillimeter Wavelengths*, vol. 217, pp. 11–18, December 1999. 31
- [24] R. S. Elliott, *Antenna Theory and Design*. IEEE Press, 2003. 31
- [25] K. F. Warnick and M. A. Jensen, “Effects of mutual coupling on interference mitigation with a focal plane array,” *IEEE Transactions on Antennas and Propagation*, vol. 53, no. 8, pp. 2490–2498, August 2005. 36
- [26] G. A. Hampson and S. W. Ellingson, “A subspace-tracking approach to interference nulling for phased array-based radio telescopes,” *IEEE Transactions on Antennas and Propagation*, vol. 50, no. 1, January 2002. 69, 73
- [27] J. D. Kraus, *Radio Astronomy*, 2nd ed. Cygnus-Quasar Books, 1986. 69